

Integrating a double cropping model with groundwater-fed irrigation in the North China Plain

Yuwen FAN¹, Zhao Yang², Min-Hui Lo³, and Eun-Soon Im⁴

¹Hong Kong University of Science and Technology

²Pacific Northwest National Laboratory

³National Taiwan University

⁴The Hong Kong University of Science and Technology

November 20, 2023

Abstract

Irrigated cultivation, as a prevalent anthropogenic activity, exerts a significant influence on land use and land cover, resulting in notable modifications to land-atmosphere interaction and the hydrological cycle. Given the extensive cropland, high productivity, compact rotation, semi-arid climate, intense irrigation, and groundwater depletion in the North China Plain (NCP), the development of a comprehensive crop-irrigation-groundwater model becomes imperative for understanding agricultural-induced climate response in this region. This study presents an integrated crop model explicitly tailored to the NCP, which incorporates double-cropping rotation, irrigation practice, and groundwater interactions into the regional climate model. The modifications are implemented to: (1) enable a seamless transition from field scale application to regional scale application, facilitating the incorporation of spatial variability, (2) capture the distinctive attributes of the NCP region, ensuring the model accurately reflects its unique characteristics, and (3) reinforce the direct interaction among crop-related variables, thereby enhancing the model's capacity to simulate their dynamic behaviors. The integrated crop modeling system demonstrates a commendable performance in crop simulations using climatic conditions, which is substantiated by its identification of crop stages, estimation of field biomass, prediction of crop yield, and finally the projection of monthly leaf area index. In our next phase, this integrated crop modeling system will be employed in long-term simulations to enhance our understanding of the intricate relationship between agricultural development and climate change.

1 **Integrating a double cropping model with groundwater-fed irrigation in the North China Plain**

2
3 **Yuwen Fan¹, Zhao Yang², Min-Hui Lo³ and Eun-Soon Im^{1,4}**

4
5 ¹ Division of Environment and Sustainability, The Hong Kong University of Science and
6 Technology, Hong Kong, China

7 ² Pacific Northwest National Laboratory, Richland, WA, USA

8 ³ Department of Atmospheric Sciences, National Taiwan University, Taipei, Taiwan

9 ⁴ Department of Civil and Environmental Engineering, The Hong Kong University of Science
10 and Technology, Hong Kong, China

11
12
13
14 Corresponding author: Yuwen Fan (yfanaj@connect.ust.hk), Eun-Soon Im (ceim@ust.hk)

15
16
17 **Key Points:**

- 18
- 19 • The implementation of the widely adopted double cropping rotation allows for a significantly improved simulation of crop phenology in NCP.
 - 20 • The water-sensitive crop simulation underscores the importance of irrigation in maintaining compact rotation and high productivity in NCP.
 - 21 • The use of province-based thresholds and crop-followed applications effectively captures the spatial variability of irrigation consumption.
- 22
23
24

25 **Abstract**

26 Irrigated cultivation, as a prevalent anthropogenic activity, exerts a significant influence on
27 land use and land cover, resulting in notable modifications to land-atmosphere interaction and
28 the hydrological cycle. Given the extensive cropland, high productivity, compact rotation,
29 semi-arid climate, intense irrigation, and groundwater depletion in the North China Plain
30 (NCP), the development of a comprehensive crop-irrigation-groundwater model becomes
31 imperative for understanding agricultural-induced climate response in this region. This study
32 presents an integrated crop model explicitly tailored to the NCP, which incorporates double-
33 cropping rotation, irrigation practice, and groundwater interactions into the regional climate
34 model. The modifications are implemented to: (1) enable a seamless transition from field scale
35 application to regional scale application, facilitating the incorporation of spatial variability, (2)
36 capture the distinctive attributes of the NCP region, ensuring the model accurately reflects its
37 unique characteristics, and (3) reinforce the direct interaction among crop-related variables,
38 thereby enhancing the model's capacity to simulate their dynamic behaviors. The integrated
39 crop modeling system demonstrates a commendable performance in crop simulations using
40 climatic conditions, which is substantiated by its identification of crop stages, estimation of
41 field biomass, prediction of crop yield, and finally the projection of monthly leaf area index.
42 In our next phase, this integrated crop modeling system will be employed in long-term
43 simulations to enhance our understanding of the intricate relationship between agricultural
44 development and climate change.

45

46 **Plain Language Summary**

47 Irrigated cropping in the North China Plain (NCP) have a significant impact on the regional
48 climate and water cycle. To better understand how agriculture affects the climate in this region,
49 we developed a comprehensive crop-irrigation-groundwater model. This model specifically
50 focuses on the NCP region and includes double-cropping rotation, irrigation practices, and
51 groundwater dynamics. By comparing with the observation, the integrated model make great
52 improvement in simulating crop stages, leaf and stem mass, crop yield, and vegetation greeness.
53 In the next phase, we will use this model to study the long-term effects of agricultural
54 development on climate change in the NCP.

55

56

57

58

59

60

61

62

63 **1 Introduction**

64 Agriculture is one of the primary drivers of land use changes (Goldewijk, 2001) and the largest
65 consumer of water resources globally (Foley et al., 2011). To increase crop productivity and
66 feed the exploding population, irrigation has rapidly expanded in the past decades, and accounts
67 for over 70% of the global freshwater withdrawal today, exerting a significant influence on the
68 hydroclimate (McDermid et al., 2023; S. Siebert et al., 2010). As surface water becomes
69 increasingly scarce, groundwater is then being exploited to meet the demands of intensive
70 irrigation, particularly in semi-arid regions or during the dry season (Famiglietti, 2014; Wada
71 et al., 2012). The overexploitation of groundwater resources can lead to depletion of soil
72 moisture and freshwater availability, as well as potential disasters such as land subsidence and
73 seawater intrusion (An et al., 2021; Famiglietti, 2014). While cultivation practices gradually
74 alter the climatic processes, it is also worth noting that the changing climate also influences
75 back onto crop production (Ahmed et al., 2015; M. Yang & Wang, 2023). Hence, it is
76 imperative to incorporate the cultivation-climate interactions into the current climate models,
77 specifically into the land-surface models (LSMs), to better simulate and understand the
78 complex relationships between agriculture and climate change.

79 Although agriculture has not been explicitly represented in most regional climate models
80 (Oleson et al., 2013), few relevant schemes are already implemented. Several crop models have
81 been designed to capture the seasonal and interannual pattern of crop phenology, such as leaf
82 area index and biomass (X. Liu et al., 2016; Oleson et al., 2013; Yin & van Laar, 2005). Unlike
83 generic dynamic vegetation schemes, these crop models can identify current crop stages (e.g.,
84 emergence, reproduction) based on the climate conditions (e.g., temperature, sunshine),
85 calculate vegetation growth in different crop stages (e.g., growth rate, carbon allocation), as
86 well as simulate the human practices (e.g., planting and harvesting). Furthermore, irrigation
87 can be applied with a fixed amount (Vira et al., 2019) or dynamically based on soil conditions
88 (Ozdogan et al., 2010; Qian et al., 2013; Valayamkunnath et al., 2021; L. Wu et al., 2018; B.
89 Yang et al., 2016; Z. Yang et al., 2017, 2019, 2020), which has improved the understanding of
90 the climate response to irrigation. Although it has been generally agreed that irrigation has a
91 cooling and moistening effect globally (Cook et al., 2011; Lo et al., 2021; Pokhrel et al., 2012;
92 Puma & Cook, 2010), its influence is non-linear and location-specific at regional scales, as it
93 greatly depends on the agricultural and climatic conditions of the region in which it is deployed
94 (Yuwen Fan et al., 2023; Im et al., 2014; Kang & Eltahir, 2018, 2019; Pei et al., 2016;
95 Tuinenburg et al., 2014; Wey et al., 2015; Z. Yang et al., 2019). Independent with the crop
96 modules and irrigation schemes, some groundwater models parameterize the soil-groundwater
97 interactions such as downward drainage and capillary rise (Lo & Famiglietti, 2011; Niu et al.,
98 2007, 2011). In addition to vertical water transportation, lateral flow (Ying Fan et al., 2007;
99 Kabir et al., 2023; Miguez-Macho et al., 2007; Zeng et al., 2018) and human consumption
100 (Anderson et al., 2015; Kabir et al., 2023; L. Wang et al., 2020) have also been included in the
101 subsurface process to complete the groundwater dynamics. The implementation of the
102 groundwater sector shows its potential to reduce dry and hot biases over the central United
103 States, as groundwater replenishes the nearby river and root-zone soils (L. Wang et al., 2020).

104 Prior research has demonstrated a widespread potential for simulating cultivation including
105 crop phenology, irrigation practices, and groundwater storage. Additionally, these modules
106 have been integrated to address more complex processes. A common approach is to combine a
107 crop module with irrigation activity (Xu et al., 2019; B. Yang et al., 2016; Z. Zhang et al.,
108 2020), which has resulted in significant enhancements in crop yield predictions and a better
109 understanding of irrigation impact. Other studies have joint soil-moisture-dependent irrigation
110 with the unconfined layer (Kabir et al., 2023; Leng et al., 2014; L. Wu et al., 2018), improving
111 model performance in reproducing the latent heat and soil moisture (Wang 2020). However,
112 few studies comprehensively considered all of these factors simultaneously, especially in
113 regional climate models. Given the close and complex relationships between these processes,
114 any missing component would lead to inadequacies in representing the climatic process over
115 croplands. Therefore, there is an increasing need to develop a joint crop-irrigation-groundwater
116 model in LSMs.

117 As a key agricultural region, the North China Plain (NCP) encompasses more than 40% of
118 China's total harvested area (FAO, 2019). Approximately two-thirds of the land within the NCP
119 is dedicated to cropland, contributing to nearly half of the national wheat production and one-
120 third of the corn production (E. Wang et al., 2008). The significance of NCP for agricultural
121 study is rooted not only in its extensive cropland and high productivity, but also in its compact
122 rotation, semi-arid background, intense irrigation, and groundwater depletion, which makes the
123 NCP an ideal testbed for evaluating the integrated crop modeling system. To maintain its high
124 productivity, a double-cropping system, typically winter wheat with summer maize, is widely
125 adopted in NCP (Jiang et al., 2021). However, the annual precipitation in NCP is only around
126 800mm, which is almost half of that in southern China (Zhe et al., 2014), increasing its
127 dependency on irrigation, especially from groundwater. About 40% of the farmland on the
128 NCP is reliant on irrigation (Portmann et al., 2010; Stefan Siebert et al., 2013), with around 62%
129 of the water usage coming from underground (J. Wang et al., 2019). The relatively dry climate
130 in the NCP makes it more sensitive to the additional water induced by the intense irrigation
131 (Yuwen Fan et al., 2023), and groundwater overexploitation has led to a rapid expansion of
132 above-ground water storage, potentially causing long-term hydrological alterations (Y. Zhou
133 et al., 2022). All of these imply that the crop modelling system for the NCP region needs to
134 consider all the interactions between crop growth, irrigation practice, and groundwater usage,
135 which will have further implications for the long-term agriculture and climate in the region.

136 Given the unique characteristics of the NCP, our research aims to develop an integrated crop
137 model with irrigation and groundwater interaction, specifically tailored for the NCP and its
138 surrounding region. In light of the reasonable performance of various related schemes, the main
139 focus of this study is to combine these components together with appropriate modifications,
140 instead of reinventing new algorithms. To achieve this, Noah-Multiparameterization (Noah-
141 MP) has been selected, as it already encompasses several functions related to cultivation
142 simulation. It is conducted online with the Weather Research Forecast (WRF) to include the
143 two-way nested feedback between the crop system and climate dynamics. Moreover,
144 regionalization becomes imperative since certain schemes within Noah-MP are primarily
145 developed and calibrated based on local field observations in the United States. Although the

146 general algorithm might be applicable worldwide, the specific details or parameters may not
147 be suitable for the NCP. For instance, it is necessary to consider the prevailing practice of
148 double cropping rotation since it has the potential to greatly affect the vegetation pattern and
149 irrigation demand. Also, applying spatially varied crop calendars and irrigation thresholds
150 according to the regional-specific observation, rather than a uniform value, can greatly improve
151 crop yields and irrigation amount (Xu et al., 2019; Z. Zhang et al., 2020). And large regional
152 uncertainties may exist in some parameters such as leaf area per living leaf biomass (BIO2LAI,
153 also known as specific leaf area) (Yu et al., 2022; Z. Zhang et al., 2020). Hence, we conduct
154 parameter calibration and adopt local inputs. While regionalizing the model, the generality
155 should also be considered to ensure its potential application in other regions or other climate
156 models. By integrating and regionalizing the crop modelling system, this study primarily
157 focuses on the model development and its predictability assessment in crop phenology and
158 irrigation requirements. However, there is a great potential for applying it in long-term
159 simulation, which represents a promising avenue for advancing our understanding of the
160 coupled human-natural system.

161

162 **2 Model Description and Experiment Design**

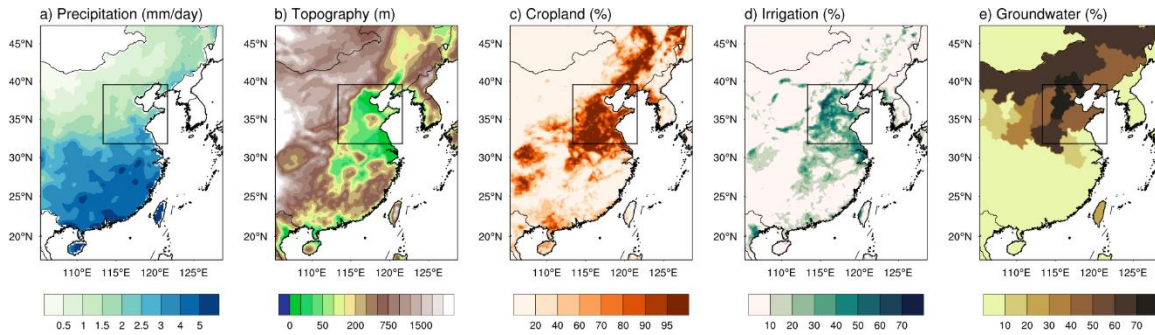
163 The study domain is centered on the NCP, encompassing a significant portion of China's
164 cropland. Considering the specific attributes of the study area, modifications are made under
165 the following conditions: (1) to facilitate the transition from field scale application to regional
166 scale application, enabling the incorporation of spatial variability, (2) to capture the local
167 specialties of the NCP region, ensuring the model accurately represents its unique
168 characteristics, (3) to complement the direct interaction among crop-related variables,
169 enhancing the model's ability to simulate their dynamics. Experiments are designed to compare
170 the model's performance with and without these modifications.

171

172 **2.1 Study Area**

173 Figure 1 illustrates some key background variables, outlining the NCP region within black
174 boxes. The topography and cropland fraction are basic geostatic inputs for the WRF, initially
175 retrieved from the United States Geological Survey and Moderate-resolution Imaging
176 Spectroradiometer (MODIS), respectively. Notably, the NCP region, being the largest plain in
177 eastern China, exhibits an average elevation even below 100m (Figure 1b), contributing to its
178 suitability for cultivation. Despite the high cropland fraction exceeding 95% in most of the
179 pluvial area (Figure 1c), the climatology annual precipitation (retrieved from China
180 Meteorological Forcing Dataset) in 2000-2009 is merely half that of southern China (Figure
181 1a), highlighting the need for irrigation. According to the FAO AQUASTAT database (Stefan
182 Siebert et al., 2013), irrigated cropland constituted more than 70% of the total land use in the
183 pluvial area in 2005 (Figure 1d). Given the scarcity of surface water in northern China,
184 groundwater plays a crucial role in meeting the substantial irrigation demand (Figure 1e).

185 Statistical data indicates that groundwater dependence in Hebei and Henan provinces reached
 186 70% and 60%, respectively (National Bureau of Statistics of China, 2005).



187 **Figure 1.** (a) Annual precipitation (mm/day) and basic geostatic variables applied in this
 188 project including (b) topography (m), (c) cropland fraction (%), (d) irrigated land fraction (%),
 189 (e) groundwater dependence (%).

190

191 2.2 Model Configuration and Experiment Design

192 The study employs the Advanced Research version of the WRF Model (version 4.3), a non-
 193 hydrostatic numerical weather prediction model that has been widely adopted in regional
 194 studies. The horizontal grid spacing is 27km, with 38 vertical layers in the atmosphere and 4
 195 soil layers below the ground. Its physical options mostly follows Fan et al. (2023), including
 196 the WRF double-moment 5-class microphysical parameterization (Hong et al., 2004), the
 197 Rapid Radiative Transfer Model as the longwave radiation scheme (Mlawer et al., 1997), the
 198 Dudhia shortwave radiation scheme (Dudhia, 1989), the Yonsei University planetary boundary
 199 layer scheme (Hong et al., 2006), the scale-aware New Simplified Arakawa-Schubert scheme
 200 (Han & Pan, 2011; Kwon & Hong, 2017), and Noah-MP land surface model coupled with our
 201 improved crop, irrigation and groundwater schemes (Ek et al., 2003). The initial and lateral
 202 boundary conditions are obtained from the ERA5 reanalysis dataset, with 6-hour output
 203 intervals, which helps to reduce the uncertainty arising from the boundary condition (Hersbach
 204 et al., 2020).

205 **Table 1.** Description of all experiments

Experiment	Model		
	Crop	Irrigation	Groundwater
CTL			
CROPdef	default version		
CROPnew	improved version		
IRRdef	improved version	default version	
IRRnew	improved version	improved version	
GWnew	improved version	improved version	improved version

206

207 We conduct multiple experiments to validate the crop growth and irrigation behaviour in 2005,
208 which has a normal value of the East Asian Summer Monsoon Index. Considering that winter
209 wheat is typically sown in the autumn of the preceding year, all experiments are started on 1
210 March 2004. This allows for a spinning-up period of at least six months prior to the 2004-2005
211 crop season, ensuring that the model was appropriately initialized for accurate simulations.
212 When examining the intra-annual pattern (e.g., monthly crop growth), we only present the
213 monthly pattern specifically in the year 2005.

214 Detailed information regarding all experiments can be found in Table 1, including the choices
215 of crop, irrigation, and groundwater models. All models are inactive in the control experiment
216 (CTL), in which static vegetation with predefined monthly patterns from satellite data is
217 employed. The crop and irrigation model can be applied either in the default version or the
218 improved version. The default crop model is conducted using the original scheme proposed by
219 Liu et al. (2016) and parameters derived from Zhang et al. (2020), while the improved crop
220 model involves both modifications to the algorithms and recalibration of the parameters. In
221 order to exclusively demonstrate the advancements made by the crop model, the irrigation
222 component remains inactive in both CROPdef and CROPnew. This implies that no
223 supplementary water is introduced to the cropland, thereby highlighting the impact solely
224 attributed to the enhancements made within the crop model. The added value of our
225 improvements on the irrigation model can be discerned through a straightforward comparison
226 between IRRdef and IRRnew experiments. In IRRdef, the default version of dynamic irrigation
227 is derived from He et al. (2023) and serves as the baseline for the improved version. In the
228 default version, the target soil moisture availability as a parameter threshold is uniformly set to
229 0.8, as suggested by Fan et al. (2023), while in the improved version, it exhibits spatial
230 variability between provinces. Finally in GWnew, we incorporate the irrigation extraction
231 process into Miguez-Macho et al. (2007) groundwater scheme, together with the improved crop
232 and irrigation model, to visualize the distinct effects on crop prediction resulting from the
233 interactions between groundwater and soil. The detailed improvements made to the crop,
234 irrigation, and groundwater models will be explained in Sections 2.3, 2.4, and 2.5, respectively.

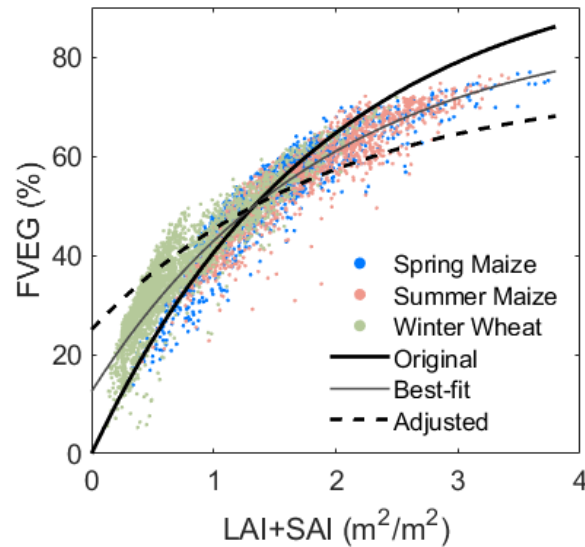
235

236 **2.3. Modification of the crop model**

237 2.3.1 Crop area and FVEG prediction

238 In order to achieve efficient computation, the crop module developed by Liu et al. (2016) is
239 selected as the foundation for crop simulation. This module operates based on the planting and
240 harvesting dates, using growing degree days (GDD) to predict the growth stages on a yearly
241 routine. The growth rate and carbohydrate accumulation are primarily influenced by factors
242 such as photosynthesis and respiration, which are sensitive to crop mass, water stress, soil
243 temperature, CO₂ concentration, and solar radiation. Then, these carbohydrates are allocated
244 among different plant components, including leaves, stems, roots, and grains, dedicated by
245 distribution schemes that vary with the growth stage. This particular crop model was initially
246 designed for crop fields and thus applied uniformly to all the grids within the domain. However,
247 to extend its application to a larger domain that has various land-use types, the model needs to
248 be exclusively activated on crop grids, while non-crop grids utilize prescribed vegetation. A

249 crop grid is defined based on MODIS land-use classification as either 'Croplands' or
250 'Cropland/Natural Vegetation Mosaic'. This definition aligns with Fan et al. (2023), and is
251 similar to the approach employed by Yu et al. (2022) who set a threshold of 50% cropland
252 percentage, since the majority of grids in the NCP region contain over 90% cropland (Figure
253 1c).



254 **Figure 2.** The relationship between FVEG and LAI+SAI in the NCP region. The thick solid
255 line presents the original empirical relationship (Equation 1), the fine solid line for the best-fit
256 relationship, and while thick dash line for the adjusted equation (Equation 2).

257 Although the dynamic leaf area index (LAI) and stem area index (SAI) can be calculated based
258 on crop growth and climate conditions, the default crop model sets the vegetation fraction
259 (FVEG) to the maximum value (i.e., 95%) for all grids, to represent the dense vegetation in the
260 crop field. However, this fixed value might not be appropriate for regional-scale applications.
261 Considering the long-term impact of FVEG variability through vegetative radiation and canopy
262 interception (W. Liu et al., 2020; D. Wang et al., 2007), we correlate FVEG with the LAI/SAI
263 using the empirical relationships (Equation 1) proposed by Niu et al. (2011) and further testified
264 by Wu et al. (2018) in the NCP region. However, according to the MODIS observation
265 retrieved from the input of the CTL, it is imperative to note that the original curve
266 underestimates the FVEG at low LAI+SAI and overestimates it at high LAI+SAI (Figure 2),
267 which poses a potential risk to the reliability of the predictions. More specifically, at the onset
268 of the crop season, accurate LAI+SAI estimation leads to an underestimation of the calculated
269 FVEG. This, in turn, results in reduced shortwave radiation intercepted by vegetation and a
270 slower rate of photosynthesis. Consequently, the leaf growth is undervalued in the next
271 timestep, and the less LAI creates a larger bias on the FVEG prediction. This positive feedback
272 continues to accumulate underestimation during subsequent iterations, and ultimately, results
273 in the failure of the entire crop season. Similarly, the curve exhibits an exaggerated FVEG
274 during the flourishing period, which easily leads to uncontrollable overgrowth. This
275 susceptibility underscores the necessity to consider and address this inherent limitation. Even
276 when employing the best-fitting curve, this issue persists for almost half of the grids. Therefore,
277 we propose a constraint on the range of FVEG, limiting it to [0.25, 0.75], instead of utilizing
278 the full range of [0, 1]. This allows for a slight overestimation in the initial stages and an

279 underestimation towards the end, ensuring a successful startup and a steady progression toward
 280 its peak. The adjustment on this equation enables the spatial and temporal variations of FVEG,
 281 as well as the vegetation responses to the irrigation application.

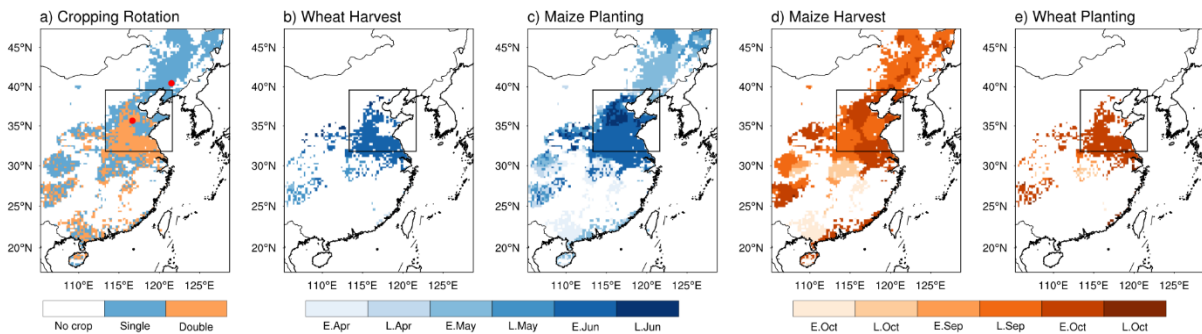
$$282 \quad \text{Original FVEG} = 1 - e^{(-0.52 \times (\text{LAI} + \text{SAI}))}, \text{FVEG} \in [0,1] \quad (1)$$

$$283 \quad \text{Adjusted FVEG} = 0.75 - 0.5 \times e^{(-0.52 \times (\text{LAI} + \text{SAI}))}, \text{FVEG} \in [0.25,0.75] \quad (2)$$

284

285 2.3.2 From single cropping to double cropping

286 The default model only considers single cropping, allowing one crop type per grid but different
 287 crops spatially. However, NCP widely adopts double-cropping rotation, as evident from
 288 satellite vegetation patterns (Qiu et al., 2022; W. Wu et al., 2010; Yan et al., 2014; Yuan et al.,
 289 2020). The first growing season typically begins in late spring to early summer and extends
 290 until mid to late autumn, followed immediately by the second growing season which stops just
 291 before the restart of the first growing season. And it's necessary to consider the second crop
 292 season in the crop-irrigation-groundwater system, because the dry soil in the winter and spring
 293 probably requires significant irrigation and groundwater supply (Yuwen Fan et al., 2023; Koch
 294 et al., 2020; L. Wu et al., 2018; B. Yang et al., 2016). According to the prevalence (Qiu et al.,
 295 2022; W. Wu et al., 2010), we select winter wheat and summer maize for double cropping
 296 region (shown in orange in Figure 3a), as identified by satellite data (Qiu et al., 2022), and
 297 spring maize for single cropping region (shown in blue in Figure 3a).



298 **Figure 3.** Spatial distribution of (a) the cropping system, (b-e) harvest date and planting date
 299 for wheat and maize over a year based on the chronological order.

300

301 The planting date and the harvesting date are fed into the crop model as the definition of the
 302 crop seasons, whose spatial variability is claimed to be beneficial to the accuracy of crop
 303 growth prediction (Xu et al., 2019; Z. Zhang et al., 2020). The harvesting date of the spring
 304 maize is assigned to be 15 days after the physiological maturity date obtained from a satellite-
 305 based post-processed dataset (Luo et al., 2020). The planting date is determined as 15 days
 306 prior to the V3 stage, which represents the early vegetative stage of maize when the third leaf
 307 is fully expanded. Similarly, for double-cropping regions, the maturity dates of wheat and
 308 maize, with a 15-day buffer, mark the end of the respective cropping seasons, while the

309 subsequent cropping season starts 5 days later. The '15-day' buffer and '5-day' interval are
310 roughly defined according to the LAI pattern in Luo et al. (2020). Few grids not covered by
311 the satellite dataset are assigned 1 May (121st Julian Day) and 11 October (284th Julian Day)
312 as the default planting and harvesting date for maize, respectively, based on field study (Yu et
313 al., 2022). The planting date and the harvesting date also perform similar spatial patterns to
314 those generated by Wu et al. (2010).

315

316 2.3.3 Input Setting and Parameter Calibration

317 We begin with the parameters for one-year corn in Bondville (Z. Zhang et al., 2020), and
318 calibrate them using data from two ChinaFlux sites, Yucheng (36.83°N, 116.57°E) for double-
319 cropping and Shenyang (41.52°N, 123.39°E) which is nearby the NCP region for single-
320 cropping, as indicated in Figure 2a. In the case of spring maize and summer maize, we first try
321 to adopt the parameters from previous studies and recalibrate if necessary, to keep the
322 generality. Conversely, a new set of parameters is developed specifically for winter wheat,
323 drawing upon statistical information from the Yucheng station, satellite datasets, and other
324 agronomy studies (Y. Zhang et al., 1991; Z. Zhang et al., 2023). Table S1 provides the adjusted
325 parameters for wheat and maize, along with the supporting scientific references. The
326 recalibration sequences are as follows.

327 The recalibration starts from crop-stage identification, since it relies purely on the accumulated
328 Growing Degrees Days (GDD) and is less affected by other crop parameters. The GDD-related
329 parameters are retrieved from Zhang et al. (2020) and Zhang et al. (1991), and then validated
330 with the heading date and maturity date retrieved from the satellite data (Luo et al., 2020). The
331 crop stage comprises the pre-planting stage, three vegetative stages (emergence, initial
332 vegetative, post-vegetative), two reproductive stages (initial reproductive, post-reproductive),
333 and finally, one maturity stage. During the vegetative stage, a majority of carbohydrates are
334 allocated to the leaves and stems, while in the reproductive stage, the allocation shifts towards
335 the grain. In our simulation results, we consider the transition date from post vegetative stage
336 to the initial reproductive stage as the heading date. This allows us to capture the transfer of
337 focus from leaf development to grain formation, aligning it with the time of maximum Leaf
338 Area Index (LAI) identified by the satellite and facilitating meaningful comparisons.

339 Next, the general growth rate including BIO2LAI can be extracted from the station data, and
340 the Maximum rate of carboxylation at 25 °C (VCMX25) can also be estimated using the
341 monthly satellite data of Gross Primary Product (GPP) and LAI, since the photosynthesis rate
342 and the LAI are approximately linearly related, especially on sunny days when the canopy
343 temperature is around 25°C (He et al., 2023). Instead of the linearly interpolated data from
344 WRF pre-processing, both GPP and LAI that we adopted are initially derived from MODIS
345 products but have undergone further post-processing to generate a more continuous monthly
346 pattern (S. Wang et al., 2020; Yuan et al., 2020), and will be considered as the observation
347 (OBS). Furthermore, the AVCMX, which represents the crop sensitivity to the temperature,
348 can be determined by the gradient of biomass accumulation (H. Huang et al., 2022), especially
349 in spring and autumn with greater temperature changes. For maize, the values of VCMX25 and

350 AVCMX have simply followed the previous studies, while BIO2LAI is subject to recalibration,
351 as its necessity of recalibration has been demonstrated by Yu et al. (2022).

352 Following the establishment of the general photosynthesis rate, we proceed to fine-tune the
353 distribution of carbohydrates among the leaf, stem, and grain compartments, based on the
354 annual cycle of leaf mass and stem data obtained from the station data. Any remaining
355 carbohydrates are allocated to the root. In cases where the recalibration of the distribution
356 scheme alone does not yield satisfactory predictions, adjustments to the turnover and
357 translocation rates are implemented. Additionally, the crop yield will be validated through
358 comparisons with remotely sensed estimations from Cheng et al. (2022).

359 Finally, the incorporation of irrigation and groundwater modules into the crop model may
360 introduce deviations in crop growth and affect the predictability of associated parameters. As
361 a result, slight adjustments are made after the integration. In essence, the crop-irrigation-
362 groundwater system, conducted in GWnew, aims to provide the most accurate simulation since
363 it reflects the closest approximation to reality.

364

365 **2.4 Modification of the irrigation model**

366 In this study focusing on the NCP, which predominantly practices dryland cultivation, the
367 irrigation methods will mostly pertain to dryland irrigation, excluding grassland irrigation and
368 paddy field irrigation. To avoid difficulties in modeling canopy interception and surface losses
369 inherent in sprinkler and fast flooding techniques, we opt for drip irrigation using the Noah-
370 MP version 5.0 model (He et al., 2023). This choice simplifies the system while maximizing
371 water resource utilization. The default irrigation module is employed from the planting date to
372 the harvesting date. In order to establish a stronger connection between irrigation and crop
373 growth, irrigation is initiated upon crop emergence and discontinued upon physiological
374 maturity. Thus, a reciprocal relationship between crop growth and irrigation is established. The
375 cooling effect resulting from irrigation extends the crop season, and in turn, requires a longer
376 irrigation period.

377 The default irrigation is activated all day all year round, which might not be realistic in large-
378 scale applications. In accordance with previous investigations, we add constraints that the
379 irrigation is implemented solely during the local time window of 6 A.M. to 10 A.M. to
380 minimize evaporative losses (Ozdogan et al., 2010; Qian et al., 2013; B. Yang et al., 2016).
381 Furthermore, the inclusion of winter cultivation necessitates the imposition of temperature
382 limitation, as irrigation under freezing conditions is deemed impractical and detrimental to
383 winter wheat (B. Yang et al., 2016). To make sure the soil is appropriate for irrigation, we
384 check whether the mean temperature of the uppermost soil layer within the preceding 24-hour
385 period exceeds 5°C. Additionally, we follow the rules from the default irrigation model that
386 the irrigation can be promptly suspended in the presence of precipitation exceeding a threshold
387 rate of 1mm/hr.

388 The default daily irrigation amount is resolved according to Equation (3) based on the soil
389 moisture and vegetation fraction which is fixed to be 0.95. When adopting it to large-scale

390 irrigation, we replace the 0.95 with the irrigation land fraction (IRRFRA) map around 2005
391 from the Food Agriculture Organization database (Stefan Siebert et al., 2013).

$$392 \quad \text{Default Irrigation Amount} = \int (\text{SMCLIM} - \text{SMCAVL}) * 0.95 \quad (3)$$

$$393 \quad \text{Improved Irrigation Amount} = \int (\text{SMCLIM} - \text{SMCAVL}) * \text{IRRFRA} \quad (4)$$

394 Irrigation is required when the soil moisture is lower than the predefined irrigation threshold
395 called management allowable deficit (MAD). MAD is a decimal number between 0 and 1,
396 indicating the cursor between the wilting and the saturated soil moisture. Soil water deficit is
397 the gap between current soil moisture availability (SMCAVL) and the expected soil moisture
398 defined by the MAD (SMCLIM). The total irrigation amount is the integrated deficit of all soil
399 layers. It is stated that the county-level calibrated irrigation threshold significantly enhances
400 the irrigation prediction (Xu et al., 2019; Z. Zhang et al., 2020). Similarly, we calibrated the
401 irrigation threshold province by province using the updated irrigation function, and finally
402 apply this MAD spatial map to IRRnew experiment. As a comparison, IRRdef only adopts 0.8
403 as a uniform threshold which is simply calibrated by the national total amount (Yuwen Fan et
404 al., 2023).

405

406 **2.5 Modification of the groundwater model**

407 Since the inclusion of lateral flow becomes crucial in predicting soil moisture in the western
408 NCP due to the steep water table gradient along the mountainous region, we select the
409 groundwater model from Miguez-Macho et al. (2007) which incorporates both water table
410 dynamics and subsurface lateral flows, and then add the irrigation extraction to it. Irrigation is
411 partially extracted from the groundwater (Equation 5) based on the reported groundwater
412 dependence of each province (Figure 1e). Since the default groundwater only updates every 30
413 minutes instead of every timestep, the accumulated extraction amount during that timeframe is
414 extracted all at once. And the groundwater table level is then recalculated based on new storage
415 as well as the soil porosity.

$$416 \quad \text{Groundwater} = \text{Groundwater} - \text{Total Irrigation} \times \text{Groundwater Dependence} (\%) \quad (5)$$

417

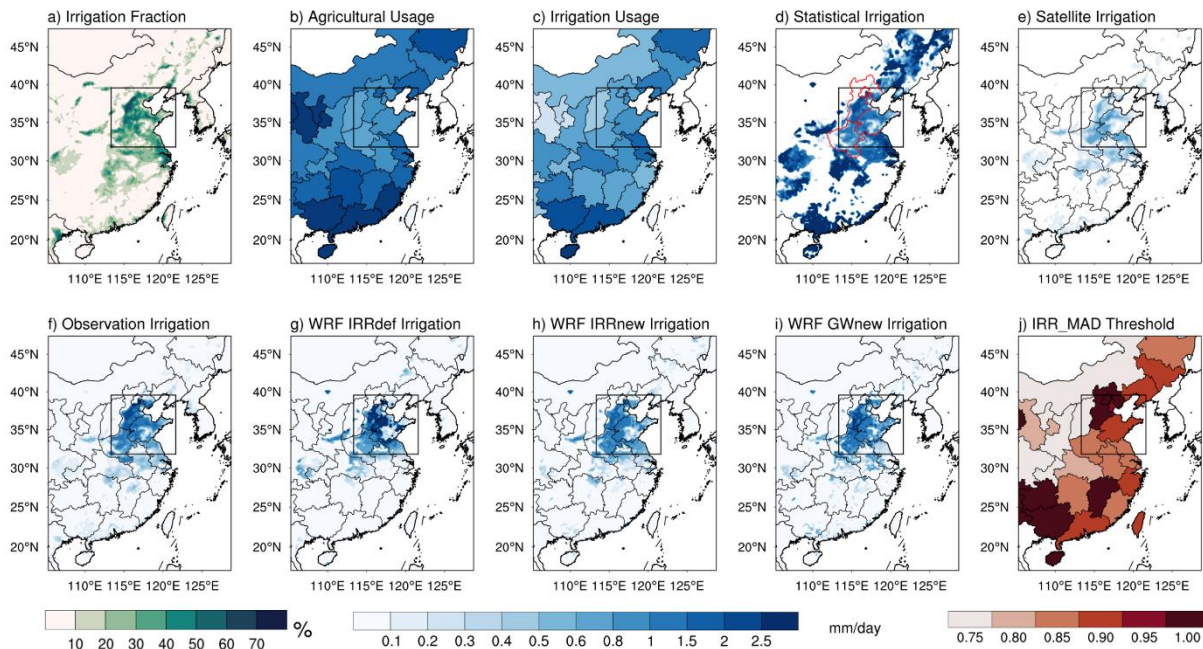
418 **3 Results**

419 **3.1 Irrigation Simulation**

420

421 It is a challenge to obtain a comprehensive and accurate observed irrigation map that covers
422 the entirety of eastern China, thus, we combine the statistical data and the satellite data,
423 considering the merged dataset as the 'observation' for calibration purposes. The statistical
424 dataset is province-based, and it was collected in 2005 which well matches our experiments.
425 However, it is provided as annual agricultural water usage which not only comprises irrigation,
426 but also husbandry, forestry, and fishery consumption (National Bureau of Statistics of China,
427 2005). So firstly, agricultural water withdrawal (Figure 4b) is converted to net irrigation (Figure

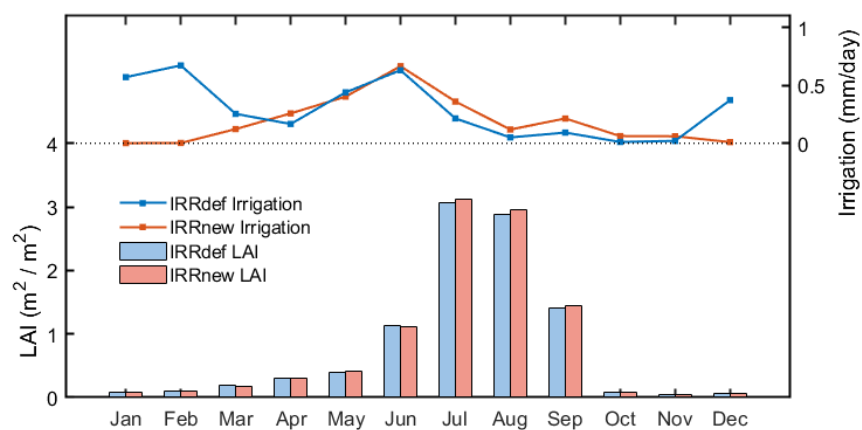
428 4c) by multiplying the provincial ratios from Zhu et al. (2012). For better visualization,
 429 irrigation is redistributed to each crop grid based on the irrigation fraction (Figure 4a). In other
 430 words, the weighted provincial mean value of the redistribution map (Figure 4d) is the same as
 431 the statistical irrigation usage (Figure 4c). Surprisingly, in Figure 4d, the annual irrigation
 432 outside the NCP, such as southern coastal region, is much more intense than that in the NCP
 433 region, probably because it includes the great consumption used for raising rice in the extensive
 434 paddy field, which is not the main focus of this study. Another satellite-based irrigation dataset
 435 contains spatial maps retrieved from water balance equations orientally. Its irrigation amount
 436 (Figure 4e) has a high similarity with the irrigation land fraction, but it only covers 2011 to
 437 2018 and it has a non-negligible underestimation (K. Zhang et al., 2022). Therefore, the
 438 statistical irrigation in the targeted NCP (i.e., Beijing, Tianjin, Hebei, Shandong, and Henan,
 439 follows D. Wu et al., 2018) is coupled with the satellite-based irrigation in other regions to be
 440 the final observation we used for calibration and validation (Figure 4f).



441 **Figure 4.** Spatial maps of (a) irrigation fraction (same as Figure 1d), (b) agricultural usage, (c)
 442 estimated irrigation usage, (d) statistical irrigation, (e) satellite irrigation, (f) observation
 443 irrigation, (g-i) simulated irrigation, and (j) MAD threshold adopted in IRRnew and GWnew

444
 445 The default irrigation scheme (Figure 4g) exhibits a tendency to overestimate irrigation in the
 446 central NCP, deviating from the observed pattern where irrigation is more prevalent in the
 447 western part along the mountain. As expected, the implementation of the spatially varied
 448 irrigation threshold demonstrates a considerable improvement (Figure 4h), closely resembling
 449 the observed spatial variability. Figure 4(j) presents the province-based MAD threshold we
 450 adopted, which is calibrated using the observation. Certain provinces in the NCP exhibit higher
 451 thresholds, even approaching 1, indicating the model's attempt to achieve near-saturation of the
 452 soil. When comparing GWnew with IRRnew, the incorporation of the groundwater scheme
 453 helps to capture the greater irrigation requirement in the mountainous region. This can be

454 attributed to the deeper groundwater table and quicker dry-down after daily irrigation. The
 455 temporal pattern clearly emphasizes the importance of incorporating soil temperature checks
 456 into the irrigation scheme. In Figure 5, the lines depict the monthly irrigation levels, while the
 457 bars represent the averaged LAI across all crop grids in the NCP region. The default irrigation
 458 scheme tends to apply excessive irrigation during the winter season, which can be attributed to
 459 the relatively drier soil conditions and thus larger gap between the soil moisture and the MAD
 460 threshold. However, despite the intense winter irrigation, the corresponding vegetation growth,
 461 as indicated by the LAI, shows insignificant improvement. And this perceived superiority of
 462 winter irrigation gradually diminishes as spring approaches. On the other hand, the improved
 463 model effectively avoids unnecessary winter irrigation, allowing for a greater allocation of
 464 water resources during the spring and summer seasons when crop growth is more pronounced.
 465 Consequently, this strategic water distribution leads to more flourishing vegetation during the
 466 summer season. In summary, the improved model provides enhanced water support to the crops
 467 while also conserving irrigation consumption on an annual basis.



468 **Figure 5.** Monthly irrigation (lines) and LAI (bars) from IRRdef, IRRnew and GWnew. Only
 469 crop grids in the NCP are counted.

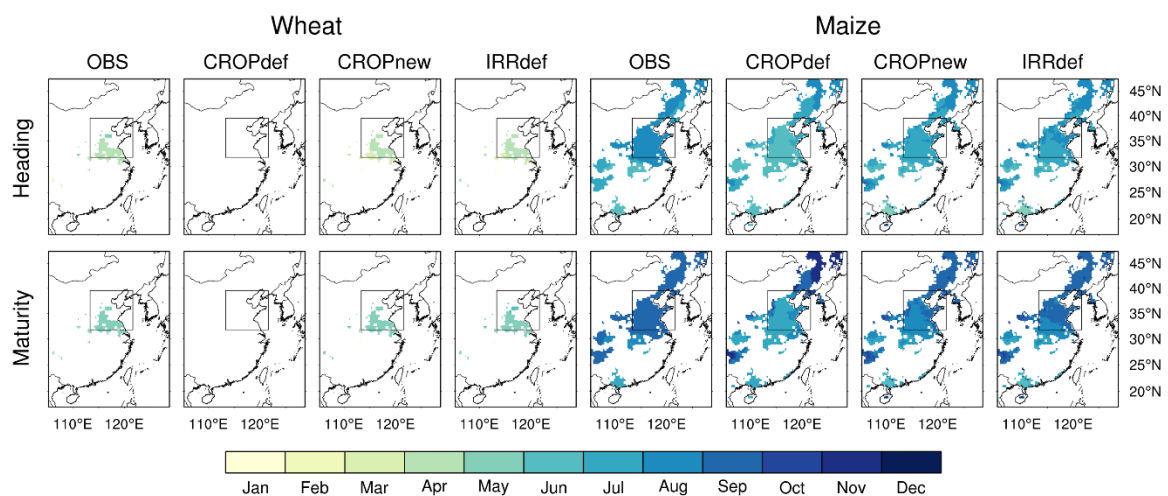
470

471 3.2 Evaluation of crop growth

472 The evaluation of the crop simulation encompasses several key aspects, including crop stage
 473 identification, annual cycle of leaf and stem mass, crop yield prediction, and general LAI
 474 simulation. These components will be scrutinized to assess the accuracy and validity of the
 475 crop model.

476 As mentioned, the heading and maturity dates serve as indicators of the transition from the
 477 vegetative stage to the reproductive stage, and ultimately to the maturity stage. We compare
 478 the heading and maturity dates of winter wheat and maize, including both summer maize and
 479 spring maize, from each simulation with the estimations derived from MODIS (Figure 6).
 480 Typically, winter wheat heads in March and matures in May, while maize heads in August and
 481 matures in September. The default crop model only considers single cropping without winter
 482 wheat. Moreover, the heading date of CROPdef is observed to be one or two months earlier
 483 than the observations, and the maturity date also exhibits deviations, being earlier in the NCP

484 but later in Northeast China. This suggests that employing a uniform starting and ending time
 485 is not suitable for a regional domain. The enhanced crop model, CROPnew, incorporates
 486 double cropping and spatially varied planting and harvesting dates, resulting in the presence of
 487 two seasons with a more accurate duration. This is because the adjustment allows for an earlier
 488 seeding and longer growing season for spring maize in the northern region, enabling the
 489 accumulation of the same Growing Degree Days (GDD) by the maturity season. The early bias
 490 is further mitigated by irrigation, as the presence of moist soil induces primary cooling,
 491 subsequently decelerating GDD accumulation and postponing the growth stage. Furthermore,
 492 the improvements made to the irrigation module and the integration of groundwater interaction
 493 slightly enhance the stage identification process, which is presented in the extended version of
 494 stage validation that includes all experiments (Figure S1).

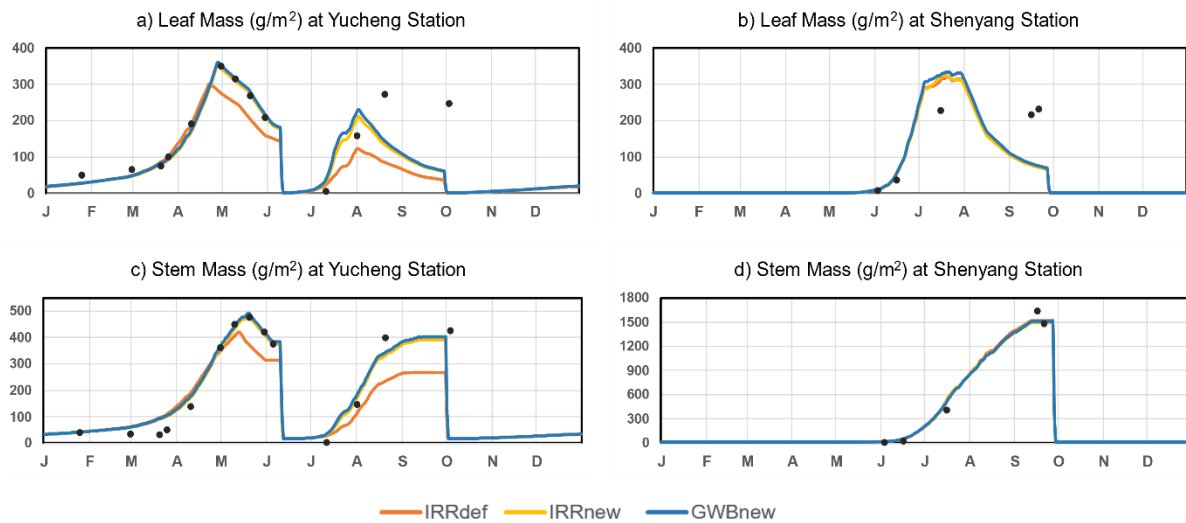


495 **Figure 6.** Validation of the crop stage identification by comparing the wheat heading date,
 496 wheat maturity date, maize heading date, maize maturity date between the simulations and
 497 the observation

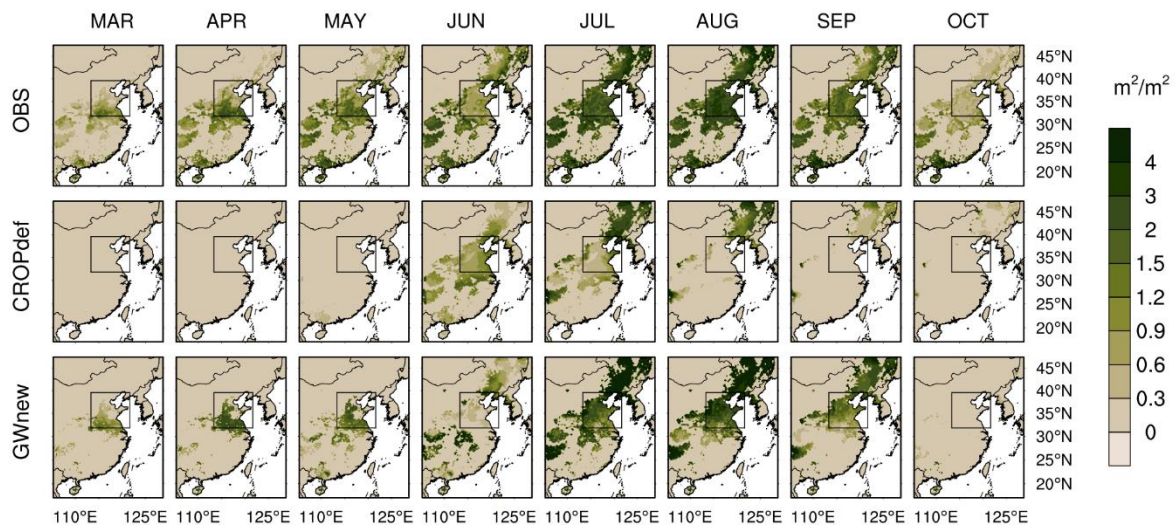
498

499 When examining the annual biomass of the Yucheng station (Figure 7a and 7c), the biomass
 500 cycle exhibits two distinct peaks, representing two crop seasons. In alignment with Figure 6,
 501 applying irrigation extends the winter wheat growth, moving the peak to the right side and
 502 resulting in a better match with the observation. Furthermore, the upgrades of the irrigation
 503 model led to significant enhancements at the Yucheng station, particularly for summer maize.
 504 This aligns with the conclusions drawn from Figure 5, as well as the suboptimal maize growth
 505 under water stress conditions captured by another crop model (Song & Jin, 2020), further
 506 approving the positive influence of the improved irrigation model on crop growth. On the other
 507 hand, irrigation is not intensely adopted in northeast China, and thus, does not make a
 508 noticeable impact at Shenyang Station (Figure 7b and 7d). In addition, the impact of
 509 groundwater integration is not particularly pronounced in both stations, probably because
 510 groundwater impact is usually considered a long-term effect, and the one-year duration may
 511 not be sufficient to fully demonstrate its impact. And the 27km grid spacing may be insufficient

512 to capture the lateral dynamics of groundwater (Barlage et al., 2021), thus limiting the
 513 manifestation of groundwater's effect.



514 **Figure 7.** Validation of the annual cycle of leaf mass and stem mass at (a, c) Yucheng Station
 515 and (b, d) Shenyang Station. Dots represent station observation and lines are the simulation
 516 results.

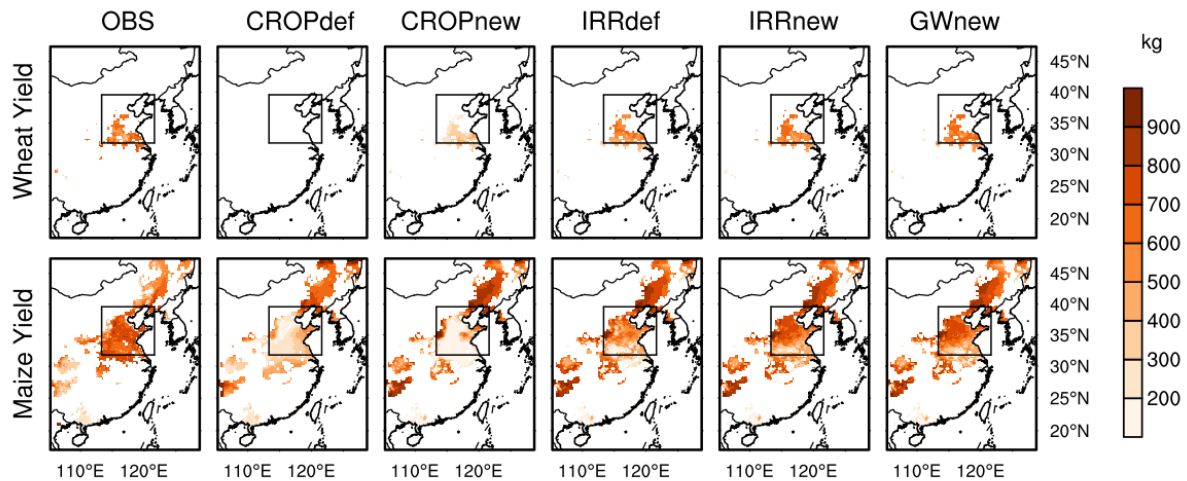


517 **Figure 8.** Validation of crop yield of wheat and maize.

518

519 By assessing the crop yield prediction in Figure 8, we can observe the progressive
 520 improvements achieved through model modification. The initial CROPdef only considers a
 521 single crop type, and it proves to be inadequate for the heavily irrigated NCP region, even with
 522 the exaggerated assumption of a fixed FVEG value of 0.95. Despite the recalibration of
 523 parameters and adjustments to the planting and harvesting dates, which realizes the double
 524 cropping simulations in the CROPnew, production in the NCP region is still severely hindered
 525 by the limited water availability. The activation of the default irrigation module in IRRdef,
 526 despite some imperfections, significantly promotes crop growth. This highlights the

527 importance of irrigation in sustaining the compact rotation and high productivity in the NCP.
 528 On the other hand, irrigation impact in northeast China is not as significant as that in the NCP,
 529 which aligns with the fact that the majority of the cropland in northeast China is rainfed. Similar
 530 to Figure 7, the improvement in irrigation practices further enhances crop yields, particularly
 531 for summer maize. The integration of groundwater results in only marginal improvement in the
 532 double cropping of summer corn, while it does not cause any significant deviations in the single
 533 cropping station.



534 **Figure 9.** Monthly LAI pattern of the satellite observation, default crop model only, and after
 535 all modification and integration.

536

537 Finally, the validation of monthly LAI as an indicator of overall vegetation growth is essential,
 538 as its accuracy plays a crucial role in determining land-atmosphere interaction and energy
 539 partitioning (X. Liu et al., 2016). Figure 9 compares the simplest crop model and the final
 540 integrated system with observation, emphasizing the remarkable improvement achieved
 541 through the integration and regionalization processes. Figure S2 provides an extended version
 542 inclusive of all experiments, thoroughly visualizing the gradual improvement made by each
 543 step. The observed LAI demonstrates a gradual increase until May, with a slight decline in June,
 544 indicating the harvest of winter wheat. In the second crop season, there is a notable rise in LAI
 545 during July and August, reflecting substantial growth and vegetation development during this
 546 period, followed by a gradual decline in September and October. It becomes evident that the
 547 CROPdef lacks representation of the first crop season and exhibits an early and truncated
 548 second crop season in the NCP. The inclusion of irrigation, both in the IRRdef and IRRnew
 549 models, significantly enhances crop growth in the double cropping region, highlighting the
 550 crucial role of irrigation in this region. Conversely, the crops in Northeast China, where rain-
 551 fed agriculture predominates, exhibit reasonably satisfactory growth even without irrigation.
 552 This regional disparity in crop sensitivity to irrigation can be aptly captured by the improved
 553 system. In line with the previous figures, the IRRnew proves particularly beneficial for the
 554 growth of summer maize. Its avoidance of unnecessary irrigation during the freezing winter
 555 months allows for greater resource allocation during the productive summer period, resulting
 556 in improved growth and development. Generally, the GWnew simulation successfully captures

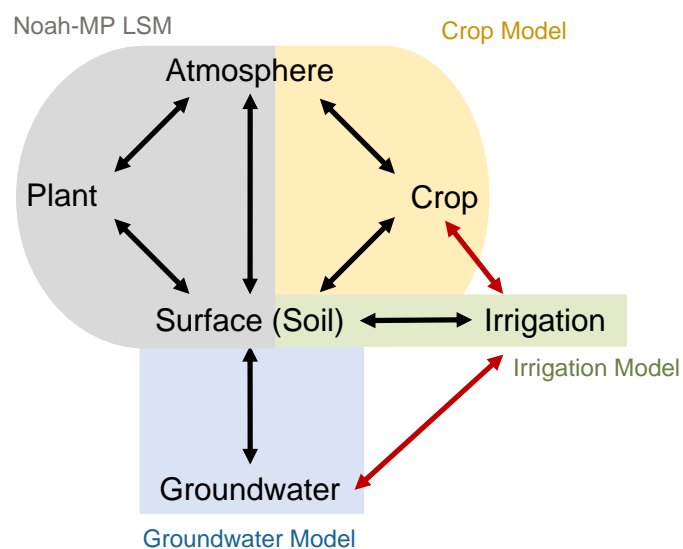
557 the spatial and temporal LAI patterns, particularly in the NCP region, which demonstrates a
 558 superior capability in accurately representing the dynamics of crop growth compared to the
 559 initial crop model, which lacked regionalization and integration. In addition to the LAI, the
 560 joint crop modelling system also demonstrates reasonable predictability in monthly FVEG
 561 (Figure S3). Consequently, this expanded functionality offers valuable opportunities to conduct
 562 sensitivity tests, enabling a deeper understanding of the agriculture-related climate response.

563

564 **4 Discussion and conclusion**

565 Considering the close and complex connections between crop growth, irrigation application
 566 and groundwater interaction in the NCP, the development of a comprehensive crop-irrigation-
 567 groundwater model becomes necessary for accurate prediction of crop growth in this region.
 568 The objective of this study is to create an integrated crop model that incorporates irrigation and
 569 groundwater interactions in the regional climate model, specifically designed for the NCP and
 570 its surrounding areas. The inclusion of the prevalent double cropping rotation enables a much
 571 more accurate simulation of plant phenology and irrigation practices. This improved system
 572 can further be applied in long-term simulations to understand the agricultural-related climate
 573 response.

574 The interconnections between the various models are depicted in Figure 10. In the default
 575 Noah-MP Land Surface Model (LSM), all modules are linked with the surface soil, but direct
 576 connections between them are absent. By introducing direct interactions between these
 577 schemes and regionalizing the functions and parameters, the integrated crop modelling system
 578 demonstrates its overall reasonable ability to predict crop production based on climatic
 579 conditions. This is validated through the accurate identification of crop stages, field point
 580 biomass estimation, crop yield prediction, and the monthly LAI pattern. The integration of
 581 these components enhances the model's predictability and allows for a more comprehensive
 582 understanding of crop growth dynamics in the NCP.



583 **Figure 10.** How models are connected. Red arrows are new connections added in this study.

584 Nevertheless, the validation process has brought to light several limitations of the current
585 model. To start with, the model design restricts the simulation of only one crop type per grid.
586 This simplification may contribute to inaccuracies in predicting the leaf mass of summer maize
587 at the Yucheng Station, which can be revealed by the inconsistency of LAI observation (Figure
588 9) in the NCP region and the leaf mass at the Yucheng Station (Figure 7). While the LAI values
589 indicate that September should have a smaller LAI compared to July, the station data suggests
590 that September actually has a greater leaf mass than July. This discrepancy can be attributed to
591 two factors. Firstly, the specific leaf area, or BIO2LAI in the model, varies across different
592 crop stages, as supported by both station data and existing literature (Amanullah, 2015; H.
593 Zhou et al., 2020). In other words, the leaves may be thinner and broader in July, while they
594 become thicker and heavier in September. The second reason is that the observed LAI pattern
595 represents a spatial average value over the grid, which may contain a diverse range of crops.
596 Consequently, the specific station data for summer maize may not align well with the spatially
597 averaged LAI. Since this study primarily focuses on the regional scale rather than individual
598 field points, we prioritize matching the spatial LAI pattern while partially sacrificing the
599 accuracy in predicting station leaf mass. As a result, the simulated LAI pattern is well-matched
600 in the NCP region, while the predicted leaf mass for summer maize may not closely align with
601 the station data. On the contrary, winter wheat greatly, even exclusively dominates the first
602 crop season, and thus the station data and spatial pattern are consistent and can both be captured
603 by the model. Also, the predicted LAI completely cleared up after harvesting, since each grid
604 can only predict one type of growth pattern, which is different from the gradual fading observed
605 in June and October.

606 Additionally, it is important to acknowledge that the model performance may be less
607 satisfactory in regions outside the primary focus of the NCP. There is some underestimation of
608 LAI and yield in the southern boundary of the NCP, as well as the overestimation in northeast
609 China. This could potentially be attributed to the limited predictability of FVEG. Also,
610 considering their different crop rotations and crop types to the NCP, the current crop system
611 may not be adequate to capture the LAI dynamics in the south coastal region and southwest
612 China. Even in regions where the model currently exhibits reasonable performance, uncertainty
613 can arise from the model's sensitivity to soil moisture (G. Wang, 2005). For instance, this study
614 only conducts experiments in a normal year, its performance in dry years or wet years needs to
615 be further tested.

616 Overall, our study has already demonstrated reasonable performance of this regional-scale
617 application in somewhere with a totally distinct climate background from the central US, where
618 the model originally developed. This implies the potential for applying it in other agricultural
619 zones. And most of our validation data is derived from satellite observations, indicating the
620 possibility of adopting it in regions even with limited ground-based data. Also, the integrated
621 crop system clearly highlights the significance of an appropriate irrigation scheme in the NCP
622 region. The inclusion of the groundwater model enables a more precise representation of the
623 spatial irrigation pattern, particularly along the mountain where irrigation is more intensified.
624 However, it does not yield significant differences, particularly in terms of crop growth.
625 Nevertheless, it is crucial to note that within the span of one year, the water exchange between

626 the soil and groundwater already influences the irrigation pattern, suggesting that over a longer
627 period, as groundwater gradually depletes, there may be more substantial changes in the
628 hydrological cycle. Further research will focus on utilizing this crop system in long-term
629 simulations, with an emphasis on investigating the cultivation-induced climate impacts and
630 hydrological changes, including groundwater storage.

631

632 **Acknowledgments**

633 This study was supported by the Hong Kong Research Grants Council funded project,
634 GRF16309719. We would like to give special thanks to Dr. Ben Yang for providing his
635 irrigation model as a reference.

636

637 **Data Availability Statement**

638 The climatology precipitation is retrieved from the China Meteorological Forcing Dataset and
639 is adopted for precipitation validation. It is produced by Cold and Arid Regions Science Data
640 Center, with doi:10.3972/westdc.002.2014.db, published at <http://westdc.westgis.ac.cn>. East
641 Asian Summer Monsoon Index is referred to <http://lijianping.cn/dct/page/65577>, with the
642 definition from Li and Zeng (Li & Zeng, 2002). LAI dataset is initially Sun Yat-sen University
643 (Yuan et al., 2020), shown at http://globalchange.bnu.edu.cn/data/global_lai_0.1/. The
644 cropping pattern is defined by ChinaCP (Qiu et al., 2022), available at
645 <https://doi.org/10.6084/m9.figshare.14936052>. The planting and harvesting date is from the
646 ChinaCropPhen1km dataset (Luo et al., 2020) at <https://doi.org/10.6084/m9.figshare.8313530>.
647 Station data at Yucheng and Shenyang is provided by the National Ecosystem Research
648 Network of China, and the yield data (Cheng et al., 2022) is freely available from
649 <https://doi.org/10.5281/zenodo.5121842>.

650

651 **References**

- 652 Ahmed, K. F., Wang, G., Yu, M., Koo, J., & You, L. (2015). Potential impact of climate change
653 on cereal crop yield in West Africa. *Climatic Change*, 133(2), 321–334.
654 <https://doi.org/10.1007/s10584-015-1462-7>
- 655 Amanullah. (2015). Specific Leaf Area and Specific Leaf Weight in Small Grain Crops Wheat,
656 Rye, Barley, and Oats Differ at Various Growth Stages and NPK Source. *Journal of*
657 *Plant Nutrition*, 38(11), 1694–1708. <https://doi.org/10.1080/01904167.2015.1017051>
- 658 An, L., Wang, J., Huang, J., Pokhrel, Y., Hugonnet, R., Wada, Y., et al. (2021). Divergent
659 Causes of Terrestrial Water Storage Decline Between Drylands and Humid Regions
660 Globally. *Geophysical Research Letters*, 48(23), e2021GL095035.
661 <https://doi.org/10.1029/2021GL095035>
- 662 Anderson, R. G., Lo, M.-H., Swenson, S., Famiglietti, J. S., Tang, Q., Skaggs, T. H., et al.
663 (2015). Using satellite-based estimates of evapotranspiration and groundwater changes

664 to determine anthropogenic water fluxes in land surface models. *Geoscientific Model*
665 *Development*, 8(10), 3021–3031. <https://doi.org/10.5194/gmd-8-3021-2015>

666 Barlage, M., Chen, F., Rasmussen, R., Zhang, Z., & Miguez-Macho, G. (2021). The
667 Importance of Scale-Dependent Groundwater Processes in Land-Atmosphere
668 Interactions Over the Central United States. *Geophysical Research Letters*, 48(5),
669 e2020GL092171. <https://doi.org/10.1029/2020GL092171>

670 Cheng, M., Jiao, X., Shi, L., Penuelas, J., Kumar, L., Nie, C., et al. (2022). High-resolution
671 crop yield and water productivity dataset generated using random forest and remote
672 sensing. *Scientific Data*, 9(1), 641. <https://doi.org/10.1038/s41597-022-01761-0>

673 Cook, B. I., Puma, M. J., & Krakauer, N. Y. (2011). Irrigation induced surface cooling in the
674 context of modern and increased greenhouse gas forcing. *Climate Dynamics*, 37(7–8),
675 1587–1600. <https://doi.org/10.1007/s00382-010-0932-x>

676 Dudhia, J. (1989). Numerical Study of Convection Observed during the Winter Monsoon
677 Experiment Using a Mesoscale Two-Dimensional Model. *Journal of the Atmospheric*
678 *Sciences*, 46(20), 3077–3107. [https://doi.org/10.1175/1520-](https://doi.org/10.1175/1520-0469(1989)046<3077:NSOCOD>2.0.CO;2)
679 [0469\(1989\)046<3077:NSOCOD>2.0.CO;2](https://doi.org/10.1175/1520-0469(1989)046<3077:NSOCOD>2.0.CO;2)

680 Ek, M. B., Mitchell, K. E., Lin, Y., Rogers, E., Grunmann, P., Koren, V., et al. (2003).
681 Implementation of Noah land surface model advances in the National Centers for
682 Environmental Prediction operational mesoscale Eta model. *Journal of Geophysical*
683 *Research: Atmospheres*, 108(D22), 2002JD003296.
684 <https://doi.org/10.1029/2002JD003296>

685 Famiglietti, J. S. (2014). The global groundwater crisis. *Nature Climate Change*, 4(11), 945–
686 948. <https://doi.org/10.1038/nclimate2425>

687 Fan, Ying, Miguez-Macho, G., Weaver, C. P., Walko, R., & Robock, A. (2007). Incorporating
688 water table dynamics in climate modeling: 1. Water table observations and equilibrium
689 water table simulations: WATER TABLE OBSERVATIONS. *Journal of Geophysical*
690 *Research: Atmospheres*, 112(D10). <https://doi.org/10.1029/2006JD008111>

691 Fan, Yuwen, Im, E.-S., Lan, C.-W., & Lo, M.-H. (2023). An increase in precipitation driven
692 by irrigation over the North China Plain based on RegCM and WRF simulations.
693 *Journal of Hydrometeorology*. <https://doi.org/10.1175/JHM-D-22-0131.1>

694 FAO. (2019). Food and Agriculture Organization Statistic Data. Retrieved from
695 <http://www.fao.org/faostat/en/#compare>

696 Foley, J. A., Ramankutty, N., Brauman, K. A., Cassidy, E. S., Gerber, J. S., Johnston, M., et al.
697 (2011). Solutions for a cultivated planet. *Nature*, 478(7369), 337–342.
698 <https://doi.org/10.1038/nature10452>

699 Goldewijk, K. K. (2001). Estimating global land use change over the past 300 years: The
700 HYDE Database. *Global Biogeochemical Cycles*, 15(2), 417–433.
701 <https://doi.org/10.1029/1999GB001232>

702 Han, J., & Pan, H.-L. (2011). Revision of Convection and Vertical Diffusion Schemes in the
703 NCEP Global Forecast System. *Weather and Forecasting*, 26(4), 520–533.
704 <https://doi.org/10.1175/WAF-D-10-05038.1>

705 He, C., Valayamkunnath, P., Barlage, M., Chen, F., Gochis, D., Cabell, R., et al. (2023). *The*
706 *Community Noah-MP Land Surface Modeling System Technical Description Version*
707 *5.0*. NCAR Technical Note NCAR/TN-575+ STR, doi: 10.5065/ew8g-yr95.

708 Hersbach, H., Bell, B., Berrisford, P., Hirahara, S., Horányi, A., Muñoz-Sabater, J., et al. (2020).
709 The ERA5 global reanalysis. *Quarterly Journal of the Royal Meteorological Society*,
710 146(730), 1999–2049. <https://doi.org/10.1002/qj.3803>

711 Hong, S.-Y., Dudhia, J., & Chen, S.-H. (2004). A Revised Approach to Ice Microphysical
712 Processes for the Bulk Parameterization of Clouds and Precipitation. *Monthly Weather*
713 *Review*, 132(1), 103–120. [https://doi.org/10.1175/1520-](https://doi.org/10.1175/1520-0493(2004)132<0103:ARATIM>2.0.CO;2)
714 [0493\(2004\)132<0103:ARATIM>2.0.CO;2](https://doi.org/10.1175/1520-0493(2004)132<0103:ARATIM>2.0.CO;2)

715 Hong, S.-Y., Noh, Y., & Dudhia, J. (2006). A New Vertical Diffusion Package with an Explicit
716 Treatment of Entrainment Processes. *Monthly Weather Review*, 134(9), 2318–2341.
717 <https://doi.org/10.1175/MWR3199.1>

718 Huang, H., Huang, J., Li, X., Zhuo, W., Wu, Y., Niu, Q., et al. (2022). A dataset of winter
719 wheat aboveground biomass in China during 2007–2015 based on data assimilation.
720 *Scientific Data*, 9(1), 200. <https://doi.org/10.1038/s41597-022-01305-6>

721 Huang, X., Wang, C., Hou, J., Du, C., Liu, S., Kang, J., et al. (2020). Coordination of carbon
722 and nitrogen accumulation and translocation of winter wheat plant to improve grain
723 yield and processing quality. *Scientific Reports*, 10(1), 10340.
724 <https://doi.org/10.1038/s41598-020-67343-5>

725 Im, E.-S., Marcella, M. P., & Eltahir, E. A. B. (2014). Impact of Potential Large-Scale Irrigation
726 on the West African Monsoon and Its Dependence on Location of Irrigated Area.
727 *Journal of Climate*, 27(3), 994–1009. <https://doi.org/10.1175/JCLI-D-13-00290.1>

728 Jiang, Y., Yin, X., Wang, X., Zhang, L., Lu, Z., Lei, Y., et al. (2021). Impacts of global
729 warming on the cropping systems of China under technical improvements from 1961
730 to 2016. *Agronomy Journal*, 113(1), 187–199. <https://doi.org/10.1002/agj2.20497>

731 Kabir, T., Pokhrel, Y., & Felfelani, F. (2023). Climatic and anthropogenic controls on
732 groundwater dynamics in the Mekong River Basin. *Journal of Hydrology*, 622, 129761.
733 <https://doi.org/10.1016/j.jhydrol.2023.129761>

734 Kang, S., & Eltahir, E. A. B. (2018). North China Plain threatened by deadly heatwaves due to
735 climate change and irrigation. *Nature Communications*, 9(1), 2894.
736 <https://doi.org/10.1038/s41467-018-05252-y>

737 Kang, S., & Eltahir, E. A. B. (2019). Impact of Irrigation on Regional Climate Over Eastern
738 China. *Geophysical Research Letters*, 46(10), 5499–5505.
739 <https://doi.org/10.1029/2019GL082396>

740 Koch, J., Zhang, W., Martinsen, G., He, X., & Stisen, S. (2020). Estimating Net Irrigation
741 Across the North China Plain Through Dual Modeling of Evapotranspiration. *Water*
742 *Resources Research*, 56(12). <https://doi.org/10.1029/2020WR027413>

743 Kwon, Y. C., & Hong, S.-Y. (2017). A Mass-Flux Cumulus Parameterization Scheme across
744 Gray-Zone Resolutions. *Monthly Weather Review*, 145(2), 583–598.
745 <https://doi.org/10.1175/MWR-D-16-0034.1>

746 Leng, G., Huang, M., Tang, Q., Gao, H., & Leung, L. R. (2014). Modeling the Effects of
747 Groundwater-Fed Irrigation on Terrestrial Hydrology over the Conterminous United
748 States. *Journal of Hydrometeorology*, 15(3), 957–972. [https://doi.org/10.1175/JHM-D-](https://doi.org/10.1175/JHM-D-13-049.1)
749 [13-049.1](https://doi.org/10.1175/JHM-D-13-049.1)

750 Li, J., & Zeng, Q. (2002). A unified monsoon index. *Geophysical Research Letters*, 29(8).
751 <https://doi.org/10.1029/2001GL013874>

- 752 Liu, W., Wang, G., Yu, M., Chen, H., Jiang, Y., Yang, M., & Shi, Y. (2020). Projecting the
753 future vegetation–climate system over East Asia and its RCP-dependence. *Climate*
754 *Dynamics*, 55(9–10), 2725–2742. <https://doi.org/10.1007/s00382-020-05411-2>
- 755 Liu, X., Chen, F., Barlage, M., Zhou, G., & Niyogi, D. (2016). Noah-MP-Crop: Introducing
756 dynamic crop growth in the Noah-MP land surface model: Noah-MP-Crop. *Journal of*
757 *Geophysical Research: Atmospheres*, 121(23), 13,953–13,972.
758 <https://doi.org/10.1002/2016JD025597>
- 759 Lo, M.-H., & Famiglietti, J. S. (2011). Precipitation response to land subsurface hydrologic
760 processes in atmospheric general circulation model simulations. *Journal of*
761 *Geophysical Research*, 116(D5), D05107. <https://doi.org/10.1029/2010JD015134>
- 762 Lo, M.-H., Wey, H.-W., Im, E.-S., Tang, L. I., Anderson, R. G., Wu, R.-J., et al. (2021). Intense
763 agricultural irrigation induced contrasting precipitation changes in Saudi Arabia.
764 *Environmental Research Letters*, 16(6), 064049. [https://doi.org/10.1088/1748-](https://doi.org/10.1088/1748-9326/ac002e)
765 [9326/ac002e](https://doi.org/10.1088/1748-9326/ac002e)
- 766 Luo, Y., Zhang, Z., Chen, Y., Li, Z., & Tao, F. (2020). ChinaCropPhen1km: a high-resolution
767 crop phenological dataset for three staple crops in China during 2000–2015 based on
768 leaf area index (LAI) products. *Earth System Science Data*, 12(1), 197–214.
769 <https://doi.org/10.5194/essd-12-197-2020>
- 770 Ma, Q., Cui, Z., & Huang, Y. (2006). Study on the Dry Matter Increase Allocation Ratio of
771 Winter Wheat. *Meteorological and Environmental Sciences*, (4), 50–51.
- 772 McDermid, S., Nocco, M., Lawston-Parker, P., Keune, J., Pokhrel, Y., Jain, M., et al. (2023).
773 Irrigation in the Earth system. *Nature Reviews Earth & Environment*, 4(7), 435–453.
774 <https://doi.org/10.1038/s43017-023-00438-5>
- 775 Miguez-Macho, G., Fan, Y., Weaver, C. P., Walko, R., & Robock, A. (2007). Incorporating
776 water table dynamics in climate modeling: 2. Formulation, validation, and soil moisture
777 simulation. *Journal of Geophysical Research: Atmospheres*, 112(D13), 2006JD008112.
778 <https://doi.org/10.1029/2006JD008112>
- 779 Mlawer, E. J., Taubman, S. J., Brown, P. D., Iacono, M. J., & Clough, S. A. (1997). Radiative
780 transfer for inhomogeneous atmospheres: RRTM, a validated correlated-k model for
781 the longwave. *Journal of Geophysical Research: Atmospheres*, 102(D14), 16663–
782 16682. <https://doi.org/10.1029/97JD00237>
- 783 National Bureau of Statistics of China. (2005). *China Statistical Yearbook*. Beijing. Retrieved
784 from <http://www.stats.gov.cn/tjsj/ndsj/2005/indexeh.htm>
- 785 Niu, G.-Y., Yang, Z.-L., Dickinson, R. E., Gulden, L. E., & Su, H. (2007). Development of a
786 simple groundwater model for use in climate models and evaluation with Gravity
787 Recovery and Climate Experiment data. *Journal of Geophysical Research*, 112(D7),
788 D07103. <https://doi.org/10.1029/2006JD007522>
- 789 Niu, G.-Y., Yang, Z.-L., Mitchell, K. E., Chen, F., Ek, M. B., Barlage, M., et al. (2011). The
790 community Noah land surface model with multiparameterization options (Noah-MP):
791 1. Model description and evaluation with local-scale measurements. *Journal of*
792 *Geophysical Research*, 116(D12), D12109. <https://doi.org/10.1029/2010JD015139>
- 793 Oleson, K., Lawrence, D., Bonan, G., Drewniak, B., Huang, M., Koven, C., et al. (2013).
794 *Technical description of version 4.5 of the Community Land Model (CLM)*
795 [Application/pdf] (p. 5912 KB). UCAR/NCAR. <https://doi.org/10.5065/D6RR1W7M>

796 Ozdogan, M., Rodell, M., Beaudoin, H. K., & Toll, D. L. (2010). Simulating the Effects of
797 Irrigation over the United States in a Land Surface Model Based on Satellite-Derived
798 Agricultural Data. *Journal of Hydrometeorology*, *11*(1), 171–184.
799 <https://doi.org/10.1175/2009JHM1116.1>

800 Pei, L., Moore, N., Zhong, S., Kendall, A. D., Gao, Z., & Hyndman, D. W. (2016). Effects of
801 irrigation on summer precipitation over the United States. *Journal of Climate*, *29*(10),
802 3541–3558.

803 Pokhrel, Y., Hanasaki, N., Koirala, S., Cho, J., Yeh, P. J.-F., Kim, H., et al. (2012).
804 Incorporating Anthropogenic Water Regulation Modules into a Land Surface Model.
805 *Journal of Hydrometeorology*, *13*(1), 255–269. [https://doi.org/10.1175/JHM-D-11-](https://doi.org/10.1175/JHM-D-11-013.1)
806 [013.1](https://doi.org/10.1175/JHM-D-11-013.1)

807 Portmann, F. T., Siebert, S., & Döll, P. (2010). MIRCA2000-Global monthly irrigated and
808 rainfed crop areas around the year 2000: A new high-resolution data set for agricultural
809 and hydrological modeling: MONTHLY IRRIGATED AND RAINFED CROP
810 AREAS. *Global Biogeochemical Cycles*, *24*(1), n/a-n/a.
811 <https://doi.org/10.1029/2008GB003435>

812 Puma, M. J., & Cook, B. I. (2010). Effects of irrigation on global climate during the 20th
813 century. *Journal of Geophysical Research*, *115*(D16), D16120.
814 <https://doi.org/10.1029/2010JD014122>

815 Qian, Y., Huang, M., Yang, B., & Berg, L. K. (2013). A Modeling Study of Irrigation Effects
816 on Surface Fluxes and Land–Air–Cloud Interactions in the Southern Great Plains.
817 *Journal of Hydrometeorology*, *14*(3), 700–721. [https://doi.org/10.1175/JHM-D-12-](https://doi.org/10.1175/JHM-D-12-0134.1)
818 [0134.1](https://doi.org/10.1175/JHM-D-12-0134.1)

819 Qiu, B., Hu, X., Chen, C., Tang, Z., Yang, P., Zhu, X., et al. (2022). Maps of cropping patterns
820 in China during 2015–2021. *Scientific Data*, *9*(1), 479. [https://doi.org/10.1038/s41597-](https://doi.org/10.1038/s41597-022-01589-8)
821 [022-01589-8](https://doi.org/10.1038/s41597-022-01589-8)

822 Siebert, S., Burke, J., Faures, J. M., Frenken, K., Hoogeveen, J., Döll, P., & Portmann, F. T.
823 (2010). Groundwater use for irrigation – a global inventory. *Hydrology and Earth*
824 *System Sciences*, *14*(10), 1863–1880. <https://doi.org/10.5194/hess-14-1863-2010>

825 Siebert, Stefan, Henrich, V., Frenken, K., & Burke, J. (2013). Global Map of Irrigation Areas
826 version 5 [Data set]. Rheinische Friedrich-Wilhelms-University, Bonn, Germany /
827 Food and Agriculture Organization of the United Nations.
828 <https://doi.org/10.13019/M20599>

829 Song, L., & Jin, J. (2020). Improving CERES-Maize for simulating maize growth and yield
830 under water stress conditions. *European Journal of Agronomy*, *117*, 126072.
831 <https://doi.org/10.1016/j.eja.2020.126072>

832 Tuinenburg, O. A., Hutjes, R. W. A., Stacke, T., Wiltshire, A., & Lucas-Picher, P. (2014).
833 Effects of Irrigation in India on the Atmospheric Water Budget. *Journal of*
834 *Hydrometeorology*, *15*(3), 1028–1050. <https://doi.org/10.1175/JHM-D-13-078.1>

835 Valayamkunnath, P., Chen, F., Barlage, M. J., Gochis, D. J., Franz, K. J., & Cosgrove, B. A.
836 (2021). Impact of Agriculture Management Practices on the National Water Model
837 Simulated Streamflow. Presented at the 101st American Meteorological Society
838 Annual Meeting, AMS. Retrieved from
839 <https://ams.confex.com/ams/101ANNUAL/meetingapp.cgi/Paper/383317>

- 840 Vira, J., Hess, P., Melkonian, J., & Wieder, W. R. (2019). *An improved mechanistic model for*
841 *ammonia volatilization in Earth system models: Flow of Agricultural Nitrogen, version*
842 *2 (FANv2)* (preprint). Biogeosciences. <https://doi.org/10.5194/gmd-2019-233>
- 843 Wada, Y., van Beek, L. P. H., & Bierkens, M. F. P. (2012). Nonsustainable groundwater
844 sustaining irrigation: A global assessment. *Water Resources Research*, 48(6).
845 <https://doi.org/10.1029/2011WR010562>
- 846 Wang, D., Wang, G., & Anagnostou, E. N. (2007). Evaluation of canopy interception schemes
847 in land surface models. *Journal of Hydrology*, 347(3–4), 308–318.
848 <https://doi.org/10.1016/j.jhydrol.2007.09.041>
- 849 Wang, E., Yu, Q., Wu, D., & Xia, J. (2008). Climate, agricultural production and hydrological
850 balance in the North China Plain. *International Journal of Climatology*, 28(14), 1959–
851 1970. <https://doi.org/10.1002/joc.1677>
- 852 Wang, G. (2005). Agricultural drought in a future climate: results from 15 global climate
853 models participating in the IPCC 4th assessment. *Climate Dynamics*, 25(7–8), 739–753.
854 <https://doi.org/10.1007/s00382-005-0057-9>
- 855 Wang, J., Yang, Y., Huang, J., & Adhikari, B. (2019). Adaptive irrigation measures in response
856 to extreme weather events: empirical evidence from the North China plain. *Regional*
857 *Environmental Change*, 19(4), 1009–1022. [https://doi.org/10.1007/s10113-018-1442-](https://doi.org/10.1007/s10113-018-1442-3)
858 3
- 859 Wang, L., Xie, Z., Xie, J., Zeng, Y., Liu, S., Jia, B., et al. (2020). Implementation of
860 Groundwater Lateral Flow and Human Water Regulation in CAS-FGOALS-g3.
861 *Journal of Geophysical Research: Atmospheres*, 125(18).
862 <https://doi.org/10.1029/2019JD032289>
- 863 Wang, S., Yongguang Zhang, & Weimin Ju. (2020). Long-term (1982-2018) global gross
864 primary production dataset based on NIRv [Data set]. figshare.
865 <https://doi.org/10.6084/M9.FIGSHARE.12981977.V2>
- 866 Wey, H.-W., Lo, M.-H., Lee, S.-Y., Yu, J.-Y., & Hsu, H.-H. (2015). Potential impacts of
867 wintertime soil moisture anomalies from agricultural irrigation at low latitudes on
868 regional and global climates: Remote Impact of Low-Latitude Irrigation. *Geophysical*
869 *Research Letters*, 42(20), 8605–8614. <https://doi.org/10.1002/2015GL065883>
- 870 Wu, D., Wang, C., Wang, F., Jiang, C., Huo, Z., & Wang, P. (2018). Uncertainty in Simulating
871 the Impact of Cultivar Improvement on Winter Wheat Phenology in the North China
872 Plain. *Journal of Meteorological Research*, 32(4), 636–647.
873 <https://doi.org/10.1007/s13351-018-7139-1>
- 874 Wu, L., Feng, J., & Miao, W. (2018). Simulating the Impacts of Irrigation and Dynamic
875 Vegetation Over the North China Plain on Regional Climate. *Journal of Geophysical*
876 *Research: Atmospheres*. <https://doi.org/10.1029/2017JD027784>
- 877 Wu, W., Yang, P., Tang, H., Zhou, Q., Chen, Z., & Shibasaki, R. (2010). Characterizing Spatial
878 Patterns of Phenology in Cropland of China Based on Remotely Sensed Data.
879 *Agricultural Sciences in China*, 9(1), 101–112. [https://doi.org/10.1016/S1671-](https://doi.org/10.1016/S1671-2927(09)60073-0)
880 2927(09)60073-0
- 881 Xu, X., Chen, F., Barlage, M., Gochis, D., Miao, S., & Shen, S. (2019). Lessons Learned From
882 Modeling Irrigation From Field to Regional Scales. *Journal of Advances in Modeling*
883 *Earth Systems*, 11(8), 2428–2448. <https://doi.org/10.1029/2018MS001595>

- 884 Yan, H., Xiao, X., Huang, H., Liu, J., Chen, J., & Bai, X. (2014). Multiple cropping intensity
885 in China derived from agro-meteorological observations and MODIS data. *Chinese*
886 *Geographical Science*, 24(2), 205–219. <https://doi.org/10.1007/s11769-013-0637-2>
- 887 Yang, B., Zhang, Y., Qian, Y., Tang, J., & Liu, D. (2016). Climatic effects of irrigation over
888 the Huang-Huai-Hai Plain in China simulated by the weather research and forecasting
889 model: Simulated Irrigation Effects in China. *Journal of Geophysical Research:*
890 *Atmospheres*, 121(5), 2246–2264. <https://doi.org/10.1002/2015JD023736>
- 891 Yang, M., & Wang, G. (2023). Heat stress to jeopardize crop production in the US Corn Belt
892 based on downscaled CMIP5 projections. *Agricultural Systems*, 211, 103746.
893 <https://doi.org/10.1016/j.agry.2023.103746>
- 894 Yang, Z., Dominguez, F., Zeng, X., Hu, H., Gupta, H., & Yang, B. (2017). Impact of Irrigation
895 over the California Central Valley on Regional Climate. *Journal of Hydrometeorology*,
896 18(5), 1341–1357. <https://doi.org/10.1175/JHM-D-16-0158.1>
- 897 Yang, Z., Qian, Y., Liu, Y., Berg, L. K., Hu, H., Dominguez, F., et al. (2019). Irrigation Impact
898 on Water and Energy Cycle During Dry Years Over the United States Using
899 Convection-Permitting WRF and a Dynamical Recycling Model. *Journal of*
900 *Geophysical Research: Atmospheres*, 124(21), 11220–11241.
901 <https://doi.org/10.1029/2019JD030524>
- 902 Yang, Z., Qian, Y., Liu, Y., Berg, L. K., Gustafson, W. I., Feng, Z., et al. (2020). Understanding
903 irrigation impacts on low-level jets over the Great Plains. *Climate Dynamics*, 55(3–4),
904 925–943. <https://doi.org/10.1007/s00382-020-05301-7>
- 905 Yin, X., & van Laar, H. H. (2005). *Crop Systems Dynamics: An ecophysiological simulation*
906 *model of genotype-by-environment interactions*. Wageningen Academic Publishers.
- 907 Yu, L., Liu, Y., Liu, T., Yu, E., Bu, K., Jia, Q., et al. (2022). Coupling localized Noah-MP-
908 Crop model with the WRF model improved dynamic crop growth simulation across
909 Northeast China. *Computers and Electronics in Agriculture*, 201, 107323.
910 <https://doi.org/10.1016/j.compag.2022.107323>
- 911 Yuan, H., Dai, Y., & Li, S. (2020). Reprocessed MODIS Version 6 Leaf Area Index data sets
912 for land surface and climate modelling. Sun Yat-sun University.
- 913 Zeng, Y., Xie, Z., Liu, S., Xie, J., Jia, B., Qin, P., & Gao, J. (2018). Global Land Surface
914 Modeling Including Lateral Groundwater Flow. *Journal of Advances in Modeling*
915 *Earth Systems*, 10(8), 1882–1900. <https://doi.org/10.1029/2018MS001304>
- 916 Zhang, K., Li, X., Zheng, D., Zhang, L., & Zhu, G. (2022). Estimation of Global Irrigation
917 Water Use by the Integration of Multiple Satellite Observations. *Water Resources*
918 *Research*, 58(3). <https://doi.org/10.1029/2021WR030031>
- 919 Zhang, Y., Tao, B., & Tang, Z. (1991). A Simulation Model for the Growth and Development
920 of Winter Wheat 冬小麦生长发育的模拟模式. *Transactions of Atmospheric Science*
921 *南京气象学院学报*, 14(1), 113–121.
- 922 Zhang, Z., Barlage, M., Chen, F., Li, Y., Helgason, W., Xu, X., et al. (2020). Joint Modeling
923 of Crop and Irrigation in the central United States Using the Noah-MP Land Surface
924 Model. *Journal of Advances in Modeling Earth Systems*, 12(7).
925 <https://doi.org/10.1029/2020MS002159>

- 926 Zhang, Z., Li, Y., Chen, F., Harder, P., Helgason, W., Famiglietti, J., et al. (2023). Developing
927 Spring Wheat in the Noah-MP LSM (v4.4) for Growing Season Dynamics and
928 Responses to Temperature Stress. *Geoscientific Model Development Discussions*, 1–26.
929 <https://doi.org/10.5194/gmd-2022-311>
- 930 Zhe, Y., Denghua, Y. a. N., Zhiyong, Y., Jun, Y. I. N., & Yong, Y. (2014). Research on
931 temporal and spatial change of 400 mm and 800 mm rainfall contours of China in 1961-
932 2000. *水科学进展*, 25(4), 494–502.
- 933 Zhou, H., Zhou, G., He, Q., Zhou, L., Ji, Y., & Zhou, M. (2020). Environmental explanation
934 of maize specific leaf area under varying water stress regimes. *Environmental and*
935 *Experimental Botany*, 171, 103932. <https://doi.org/10.1016/j.envexpbot.2019.103932>
- 936 Zhou, Y., Dong, J., Cui, Y., Zhou, S., Li, Z., Wang, X., et al. (2022). Rapid surface water
937 expansion due to increasing artificial reservoirs and aquaculture ponds in North China
938 Plain. *Journal of Hydrology*, 608, 127637.
939 <https://doi.org/10.1016/j.jhydrol.2022.127637>
- 940 Zhu, X., Shi, P., & Pan, Y. (2012). Development of a gridded dataset of annual irrigation water
941 withdrawal in China. In *2012 First International Conference on Agro- Geoinformatics*
942 *(Agro-Geoinformatics)* (pp. 1–6). Shanghai, China: IEEE.
943 <https://doi.org/10.1109/Agro-Geoinformatics.2012.6311667>

945 **Table 1.** Description of all experiments

946 **Figure 4.** (a) Annual precipitation (mm/day) and basic geostatic variables applied in this
947 project including (b) topography (m), (c) cropland fraction (%), (d) irrigated land fraction (%),
948 (e) groundwater dependence (%).

949 **Figure 5.** The relationship between FVEG and LAI+SAI in the NCP region. Thick solid line
950 presents the original empirical relationship (Equation 1), fine solid line for best-fit relationship,
951 while thick dash line for the adjusted equation (Equation 2).

952 **Figure 6.** Spatial distribution of (a) the cropping system, (b-e) harvest date and planting date
953 for wheat and maize over a year based on the chronological order.

954 **Figure 4.** Spatial maps of (a) irrigation fraction (same as Figure 1d), (b) agricultural usage, (c)
955 estimated irrigation usage, (d) statistical irrigation, (e) satellite irrigation, (f) observation
956 irrigation, (g-i) simulated irrigation, and (j) MAD threshold adopted in IRRnew and GWnew.

957 **Figure 5.** Monthly irrigation (lines) and LAI (bars) from IRRdef, IRRnew and GWnew. Only
958 crop grids in the NCP are counted.

959 **Figure 6.** Validation of the crop stage identification by comparing the wheat heading date,
960 wheat maturity date, maize heading date, maize maturity date between the simulations and the
961 observation

962 **Figure 7.** Validation of the annual cycle of leaf mass and stem mass at (a, c) Yucheng Station
963 and (b, d) Shenyang Station. Dots represent station observation and lines are the simulation
964 results.

965 **Figure 8.** Validation of crop yield of wheat and maize.

966 **Figure 9.** Monthly LAI pattern of the satellite observation, default crop model only, and after
967 all modification and integration.

968 **Figure 10.** How models are connected. Red arrows are new connections added in this study.

969

970 **Supplementary**

971 **Table S1.** Parameter setting for spring maize and summer maize.

	Same as the parameter for one-year corn from Liu et al. (2016)
	Same as the parameter for one-year corn from Z. Zhang et al. (2020)
	Same as the parameter for spring wheat from Z. Zhang et al. (2023)
	Based on winter wheat study from Y. Zhang et al. (1991)
	Recalibrated with the station/satellite data

972

Parameter	Maize		Wheat Winter	Physical meaning
	Spring	Summer		
GDDTBASE	10		0	Base temperature for GDD accumulation
GDDTCUT	30		30	Upper temperature for GDD accumulation
GDDS1	50		150	GDD from seeding to emergence
GDDS2	625		790	GDD from seeding to initial vegetative
GDDS3	1000		1190	GDD from seeding to post vegetative
GDDS4	1103		1600	GDD from seeding to initial reproductive
GDDS5	1555		2010	GDD from seeding to physical maturity
C3PSN	0		1	Indicator for C3 plant (1) or C4 plant (0)
KC25	30		30	CO ₂ Michaelis-Menten constant at 25 °C
AKC	2.1		2.1	Q10* base for KC25
KO25	3.E4		3.E4	CO ₂ Michaelis-Menten constant at 25 °C
AKO	1.2		1.2	Q10* base for KO25
AVCMX	2.4		1.5	Q10* base for VCMX25
VCMX25	60		80	Maximum rate of carboxylation at 25 °C
BP	4.E3		1.E4	Minimum leaf conductance
MP	4		9	Slope of conductance-to-photosynthesis
QE25 ⁽¹⁾	0.08		0.12	Quantum efficiency at 25 °C
Q10MR	2.0		2.0	Q10* base for maintenance respiration
LEFREEZ	268		268	characteristic T for leaf freezing
DILE_FC_S5	0.5		0.5	Coefficient for temperature leaf stress death
DILE_FC_S6	0.5		0.5	
DILE_FW_S5	0.2		0.2	Coefficient for water leaf stress death
DILE_FW_S6	0.2		0.2	
FRA_GR	0.2		0.2	Fraction of growth respiration
LF_OVRC_S5	0.2		0.05	Fraction of leaf turnover
LF_OVRC_S6	0.3		0.05	
ST_OVRC_S5	0.12		0.05	Fraction of stem turnover
ST_OVRC_S6	0.06		0.05	
RT_OVRC_S5	0.12		0.12	Fraction of root turnover
RT_OVRC_S6	0.06		0.06	

LFMR25	0.8		0.8	Leaf maintenance respiration at 25 °C
STMR25	0.05		0	Stem maintenance respiration at 25 °C
RTMR25	0.05		0	Root maintenance respiration at 25 °C
LFPT_S3	0.36	0.4	0.45	Fraction of carbohydrate flux to leaf
LFPT_S4	0.2	0.3	0.55	
LFPT_S5	0.1		0	
LFPT_S6	0.1		0	
STPT_S3	0.24	0.2	0.4	Fraction of carbohydrate flux to stem
STPT_S4	0.5	0.2	0.45	
STPT_S5	0.4	0.3	0.4	
STPT_S6	0	0.2	0.3	
RTPT_S3	0.4	0.3	0.15	Fraction of carbohydrate flux to root
RTPT_S4	0.3	0.5	0.0	
RTPT_S5	0.2	0.2	0.1	
RTPT_S6	0.1	0	0.1	
GRAINPT_S5	0.4	0.4	0.5	Fraction of carbohydrate flux to grain
GRAINPT_S6	0.8	0.7	0.6	
LFCT_S6 ⁽²⁾	0		0.0005	Carbohydrate translocation from leaf to grain
STCT_S6 ⁽²⁾	0		0.001	Carbohydrate translocation from stem to grain
BIO2LAI ⁽³⁾	0.023	0.020	0.008	Leaf area per living leaf biomass

973 *Q10 means the rate increases by a 10°C temperature increases

974 ⁽¹⁾ The QE25 parameter is increased following the removal of the great-overestimated and non-
975 water-sensitive assumption 'FVEG=0.95'. This removal significantly decreases the radiation
976 intercepted by vegetation, consequently imposing light limitations when calculating the
977 photosynthesis. Since the crop model adopts the same photosynthesis function with other non-
978 crop vegetation in the Noah-MP, for simplicity, we opt to raise the crop quantum efficiency to
979 achieve higher photosynthesis without affecting other vegetation types.

980 ⁽²⁾ Carbohydrate translocation from leaf and stem to grain, which typically occurs during the
981 reproductive stages, has been sometimes overlooked. However, we found it is necessary to
982 include it when predicting the wheat yield in the highly productive NCP (X. Huang et al., 2020;
983 Ma et al., 2006).

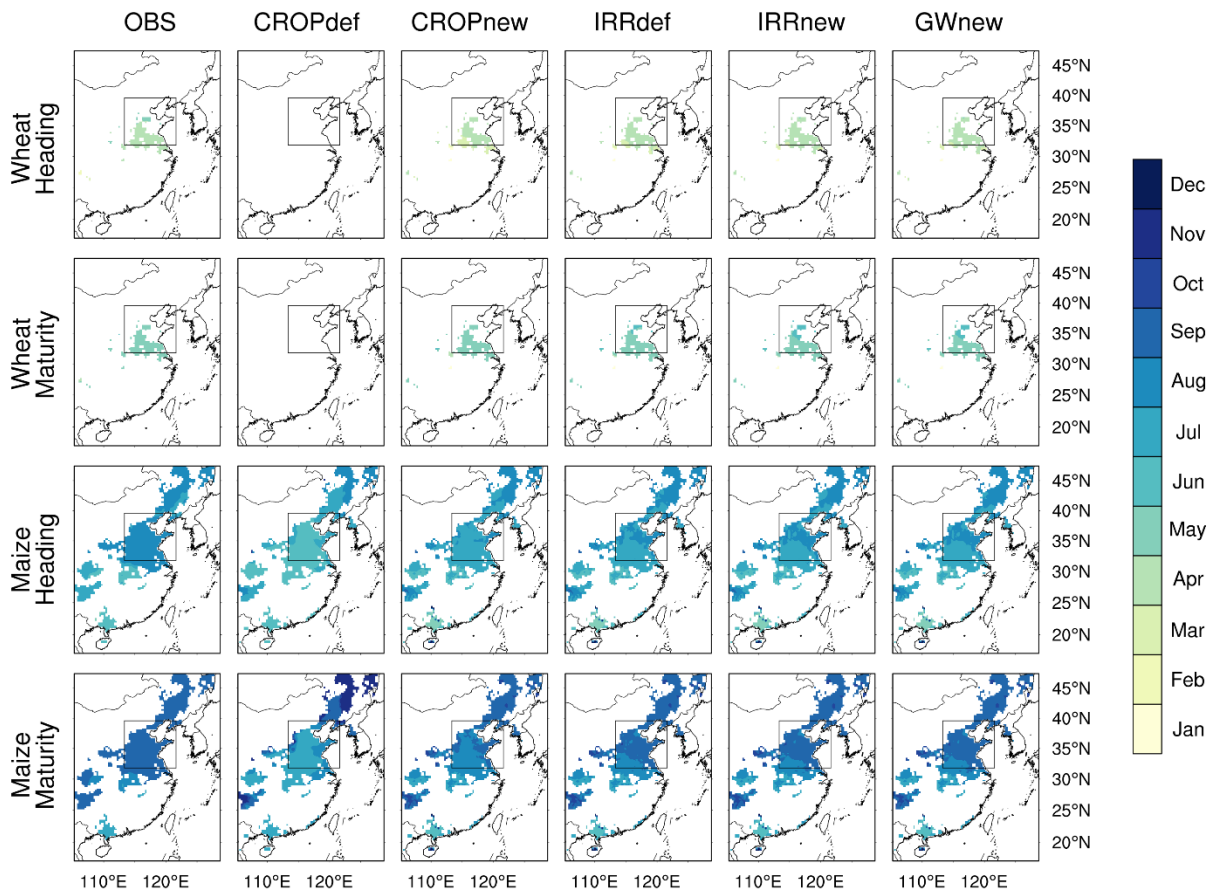
984 ⁽³⁾ The average station BIO2LAI is calculated to be 0.02 for maize and 0.01 for winter wheat
985 approximately. However, the BIO2LAI varies a lot during different stages and different
986 quadrats, which requires slightly recalibration around that station value. The final 0.023 for
987 spring maize is similar to the 0.025 calibrated by (Yu et al., 2022) in the northeast China.

988

989

990

991



992

993 **Figure S1.** Validation of the crop stage identification by comparing the wheat heading date,
994 wheat maturity date, maize heading date, maize maturity date between the simulations and the
995 observation. This is an extended version of Figure 6.

996

997

998

999

1000

1001

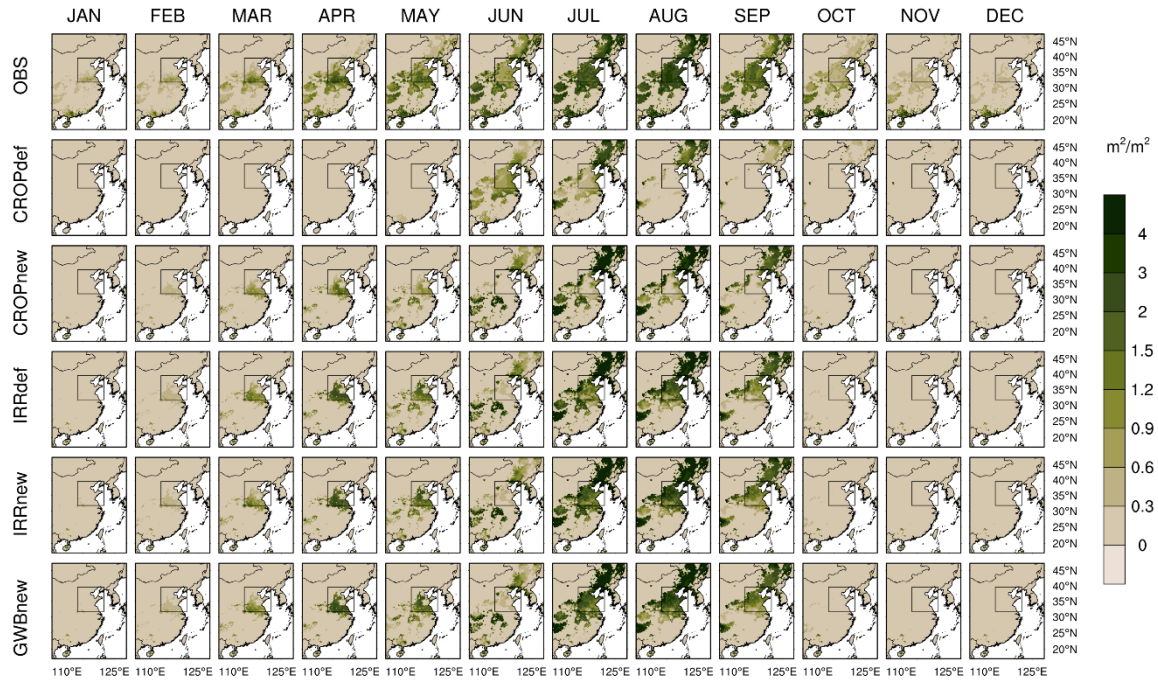
1002

1003

1004

1005

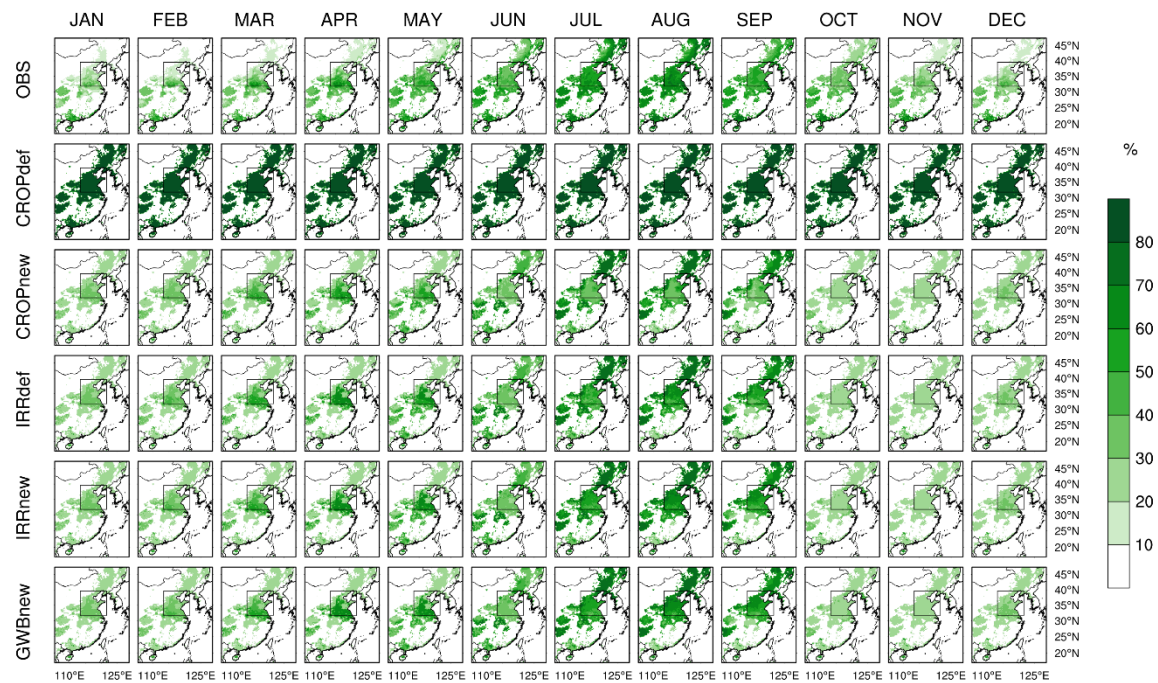
1006



1007

1008 **Figure S2.** Monthly LAI pattern of the satellite observation, default crop model only, and after
 1009 all modification and integration. This is an extended version of Figure 9.

1010



1011

1012 **Figure S3.** Similar to Figure S2 but for FVEG. Notice that in the default crop model (CROPdef)
 1013 all FVEG is fixed to 95%.